BEN-GURION UNIVERSITY OF THE NEGEV
FACULTY OF ENGINEERING SCIENCES
DEPARTMENT OF ELECTRICAL AND COMPUTER ENGINEERING

Wireless Power Transmitting Utilizing Electrical Fields

THESIS SUBMITTED IN PARTIAL FULFILLMENT OF THE
REQUIREMENTS FOR THE M.Sc. DEGREE

By: Alexander Mindel

28.02.2019

BEN-GURION UNIVERSITY OF THE NEGEV
FACULTY OF ENGINEERING SCIENCES
DEPARTMENT OF ELECTRICAL AND COMPUTER ENGINEERING

Wireless Power Transmitting Utilizing Electrical Fields

THESIS SUBMITTED IN PARTIAL FULFILLMENT OF THE REQUIREMENTS FOR THE M.Sc. DEGREE

By: Alexander Mindel

Supervised by: Professor Mor Mordechai Peretz

Author: Alexander Mindel  Date: 22/12/2019

Supervisor: Professor Mor Mordechai Peretz 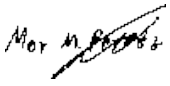 Date: 22/12/2019

Chairman of Graduate Studies Committee: …….. Date: ……..…

28.02.2019

אוניברסיטת בן-גוריון בנגב
הפקולטה למדעי ההנדסה
המחלקה להנדסת חשמל ומחשבים

מערכת תמסורת אנרגיה אלחוטית באמצעות שדות חשמליים

חיבור זה מהווה חלק מהדרישות לקבלת תואר מגיסטר בהנדסה

מאת: אלכסנדר מינדל

תאריך עברי: כ״ג באדר תשע״ט
תאריך לועזי: 28.02.2019

אוניברסיטת בן-גוריון בנגב
הפקולטה למדעי ההנדסה
המחלקה להנדסת חשמל ומחשבים

מערכת תמסורת אנרגיה אלחוטית באמצעות שדות חשמליים

חיבור זה מהווה חלק מהדרישות לקבלת תואר מגיסטר בהנדסה

מאת: אלכסנדר מינדל

מנחה: פרופסור מור מרדכי פרץ

חתימת המחבר: אלכסנדר מינדל  תאריך 22/12/2019

אישור המנחה: פרופסור מור מרדכי פרץ 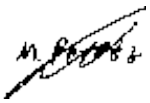 תאריך 22/12/2019

אישור יו"ר ועדת תואר שני מחלקתית..... תאריך.....

∞

Dedicated to my dear wife, Ekaterina, who encouraged me to aspire heights and ignore any limitations that got in the way, since all limitations are simply waiting there for someone to break them.

∞

תקציר

עבודה זו מציגה מערכת תמסורת אנרגיה אלחוטית באמצעות שדות חשמליים, דרך תווך קיבולי. תווך קיבולי נוצר על ידי הצבת שני זוגות לוחות מוליכים במרחב באופן בו כל זוג לוחות מאונך (לפחות בצורה מקורבת) אחד לשני, כאשר המרחק בין הלוחות פרופורציוני לגודלם, והוא כזה שיניב קיבולי אפקטיבי של פיקו-פארדים בודדים לכל הפחות בין כל זוג לוחות. אופן הפעולה דומה מאוד למערכות תמסורת אנרגיה באמצעות שדות מגנטיים הנפוצות בשוק, אך ישנם יתרונות (כגון עבודה בסביבת מוליכים) אשר הניעו את המחקר והתעשייה לבחון את מערכות תמסורת האנרגיה הקיבוליות כחלופה ראויה למערכות הקיימות.

מטרת המערכת הינה לייצר מקור זרם קבוע עבור תנאי תווך משתנים, כלומר מצב בו המרחק בין הלוחות משתנה, ו/או שטח החתך האפקטיבי שלהם משתנה. היות והתווך ניתן לייצוג באמצעות קיבולים טוריים, שינויו מתבטא בשינוי הקיבול הטורי. מכיוון שהקיבול הוא בסדר גודל של פיקו-פארדים, כל תזוזה קטנה של הלוחות יכולה להשפיע בצורה ניכרת על יכולת העברת האנרגיה של המערכת. בנוסף, אילוצי הפרויקט גם כללו מגבלות של (1) נתק גלווני מוחלט בין המשדר למקלט; (2) מתח כניסה קבוע; (3) גודל מינימלי; (4) עלות נמוכה. מכיוון שעכבת הקיבול הטורי תלויה בתדר העבודה, על מנת לשמר יכולת העברת אנרגיה ברמה הרצויה נדרש תדר עבודה העולה על מגה-הרץ. יש לציין כי שינוי הצימוד משנה את צורת אופיין תמסורת המתח/ זרם ואת מיקומו בתדר, עובדה שמקשה מאוד ליצור מערכת פיצוי אפקטיבית על סמך המגבלות.

על מנת להתגבר על אתגרים אלו, עבודה זו מציגה ממיר DC-DC תהודתי, בעלת טנקי תהודה אדפטיביים הן במשדר והן במקלט המבוססים על סליל משתנה מבוקר, אשר מזהה בצורה רציפה את כמות הזרם המועברת לעומס, ומתקנת עצמה על מנת לספק את הדרישה. התיקון מתבצע על בסיס מערכות בקרה רב-חוגיות במשדר ובמקלט הפועלות באופן בלי תלוי, וללא צורך במערכות תקשורת (עובדה המוזילה את מורכבות ועלות המערכת) על סמך ניתוח אנליטי מקדים. עבודה זו התקבלה לכנס IEEE Applied Power Electronics Conference and Exposition (APEC) 2019 [1].

מחקר זה כולל ניתוח אנליטי של מערכת העברת האנרגיה, שיטת בקרה ותוצאות ניסיונות של מדגם תחת קיבולי צימוד שונים ועומסים שונים. נמצאה התאמה גבוה בין תוצאות הניתוח האנליטי (והסימולציות הנלוות) לבין התוצאות הניסיוניות שהציג המדגם, והוכחה יכולת המערכת להעברת אנרגיה, לרבות פיצוי אקטיבי עבור תנאי צימוד שונים.

בנוסף לכך, שיטות החישה והבקרה הגנריות שפותחו במסגרת העבודה על מחקר זה מאפשרות לשלבן במערכות תמסורת אנרגיה אלחוטיות שונות (הן השראיות והן קיבוליות), בלי קשר למבנה בנק התהודה, על ידי ביצוע התאמות מינוריות בלבד. בפועל, מעבר להצגת יכולת של מערכת בודדת, מחקר זה נותן כלים תכנוניים מהירים ויעילים לפיתוח מערכות נוספות.

Abstract

This thesis presents a wireless power transmitting system utilizing electrical fields via capacitive interface. The capacitive interface is realized by placing two pairs of conducting sheets facing each other, while the spacing of the sheets in each pair proportionate to their size, such that the effective capacitance is at least a few pico-Farads [pF]. In general, the transmitting mechanism is quite similar to the wide-spread inductive power systems, although it has several advantages (working next to conductors e.g.) that led the research community and the industry to consider the Capacitive Power Transfer systems as a viable replacement for the existing wireless power transfer technologies.

The goal of the system is to create a constant current source under varying coupling conditions; the latter may be caused by changing the spacing between the sheets, or their effective overlap area. As the coupling interface can be represented by series capacitor, the coupling altering results in the series capacitance variation. As the capacitance is only a few pico-Farads, even a slight movement of the sheets may vastly affect the system's power transfer capabilities. Furthermore, the project restriction included the following: (1) complete galvanic isolation between the transmitter and receiver; (2) constant input voltage; (3) minimal overall size; (4) low cost. As the series capacitance impedance is frequency dependent, maintaining a reasonable output power dictates work frequencies that exceed 1MHz. It should be noted that any variations in the coupling change in turn the current/ voltage transfer curve's form and its location in terms of frequency, thus increasing the complexity of an active compensation system.

As a solution to the above-mentioned challenges, this paper presents a resonant DC-DC converter, with an adaptive resonant tank based on controlled varying inductor, that constantly monitors the current delivered to the load, while actively compensating in order to maintain the target current. The compensation is implemented by two independent multi-loop control systems at the transmitter and the receiver, without the need of a communication module (lowers complexity and cost), according to preliminary analysis. This paper was accepted to the IEEE Applied Power Electronics Conference and Exposition (APEC) 2019[1].

This paper includes the power transfer system's analysis, control method and experimental results of a prototype that was tested under various coupling capacitances and loads. The experimental results were found to be in good agreement with the analytic (and simulation) results, therefore confirming the potential of capacitive power transfer with active compensation under varying coupling conditions. Moreover, the generic sensing and control techniques hereby presented, enable their implementation in a vast number of wireless systems (both capacitive and inductive), regardless of the resonant tank structure. Indeed, apart from demonstrating the agility of a single system, the above paper provides simple and efficient tools for future systems development.

Keywords

Capacitive Power Transfer, Closed Loop Capacitive Wireless System, Capacitive Coupling, Impedance Matching, Self-Tuned System, Resonant Converters, Multi-loop Controller, Variable Inductor, Frequency Dithering, Active Compensation, Mixed Signal Control, Wireless Power Transfer, Analog to Digital Converter, FPGA.

Acknowledgments

I would like to thank my supervisor Prof. Mor Mordechai Peretz, with whom I worked for two and a half intensive years. Prof. Peretz has been a role model for me throughout our joint work, both personally and professionally. I owe much to his indispensable knowledge so generously shared, as well as for constantly maintaining high standards while concurrently providing assistance and instilling motivation in me. Above all, I hold his openness for mistake-making with the highest regard.

Lest I forget all the past and present students at the Center for Power Electronics and Mixed-Signal IC whose support and friendship meant so much: Dr. Alon Cervera, Mr. Eli Abramov, Mr. Timur Vekslender, Mr. Yevgeny Bezdenezhnykh, Mr. Bar Halivli, Mr. David Dayan, Mr. Tom Urkin, Mrs. Haga Perets, Mr. Guy Sovik, and anyone that I have forgotten to mention by name.

Of the technical staff, I would like to thank Dr. Michael Evzelman and Mr. Azrikam Yehieli, both responsible for the excellent working and social conditions of the laboratory.

With utmost appreciation I thank my dear wife Ekaterina; for her tremendous support, patience and care. Last but not least, I wish to thank my parents for their love, support, care and understanding.

Table of Content

Figure List

Table List

Acronyms and Abbreviations

AET - Acoustic Energy Transfer
ADC - Analog-to-digital converter
AVR - Active Variable Reactance
CPT - Capacitive Power Transfer
FB - Full Bridge
FHA - First Harmonic Approximation
FPGA - Field programmable gate array
GaN - Gallium Nitride
HILPB - High Intensity Laser Power Beam
IPT - Inductive Power Transfer
LPT - Laser Power Transmission
MPT - Microwave Power Transfer
PB - Power Beacons
UAV - Unmanned Aerial Vehicles
WPT - Wireless Power Transfer
ZCS - Zero Current Switching
ZVS - Zero Voltage Switching

1 Introduction:

1.1 Motivation:

Wireless Power Transfer (WPT) - also known as wireless charging - is a technique for transmitting electrical energy from the source to the load via air-gap, with no cord-based connection between the transmitter and the receiver. The applications of wireless power transfer technologies range from medical implants, through consumer electronics and electric vehicles, up to powering satellites. One of the significant contributors to the fast growth of both research papers and commercial applications in this field was the widespread use of portable devices (i.e. smartphones, wearable-tech) that has steadily increased over the past 20 years. In addition to the commercial potential of the WPT, which is estimated to reach 15-billion market by 2020, the improvement of power electronics' devices has rendered WPT a viable technology that can potentially serve as an alternative to power cords. In consumer electronics, the integration of WPT mostly improves the "user experience", whereas in other applications it sets the pathway for a new type of devices (i.e. med-tech). In comparison with the classic, cord-based power transfer, WPT has the following advantages:

- Improvement of user experience, as the number of cords decreases. This is similar, in a sense, to implementing WI-FI over ethernet cable.
- Dispatching electronic devices to isolated locations, in the example of medical implants or hazardous environments.
- Standardized WPT lowers the demand for various types of chargers, as devices from different manufacturers are powered by the same charger. The environmental implications for reducing the total amount of chargers are obvious.
- Device durability is improved significantly due to dust/ water proofing, by virtue of removing the external connection ports.
- Lowering or minimizing the overall system's size, by eliminating the need for power tank.

That said, however, classical wired systems have the advantage over WPT systems in terms of design/ production cost (a wire is usually cheaper than WPT system), standardization, EMI, electrical efficiency and user safety. Despite the shortcomings of WPT, it receives growing attention as a commercial opportunity and a creative approach to power devices in mobilized or isolated settings. To further promote the development and integration of WPT systems, unified standards such as Wireless Power Consortium (Qi)[2] and Air-Fuel Alliance (Alliance for Wireless Power; Power Matters Alliance)[3] set guidelines and restrictions for the designer, in a similar fashion to USB connectors for wired devices.

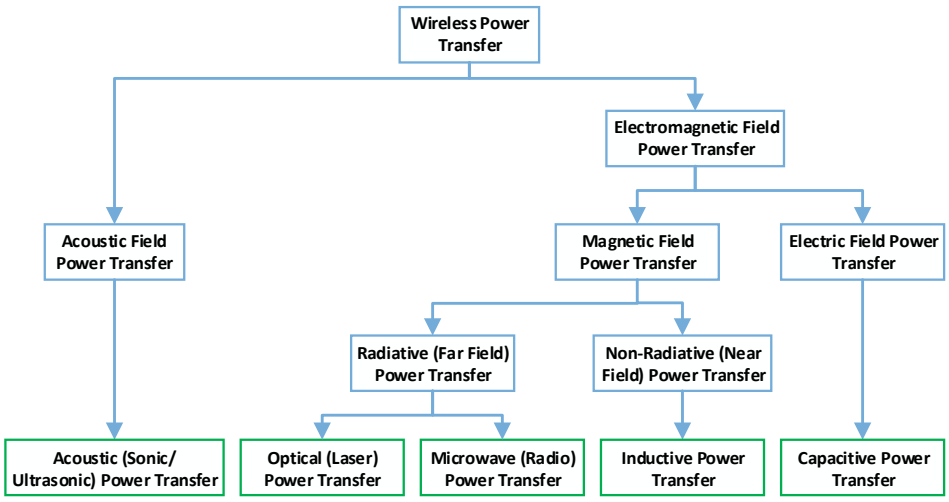

Fig. 1. Wireless Power Transfer Approaches

These standards usually dictate the wireless technology involved, frequency range, power ratings etc. The WPT systems can be categorized into two major groups: (1) near-field non-radiative wireless power transfer (coupling-based); (2) Radiative wireless power transfer (RF). Fig. 1 shows the tree-chart of the WPT approaches. The text-boxes marked green are addressed in section 1.3.

1.2 History:

The WPT history can be divided to three major phases: (1) Theoretical layout, mainly driven by the motivation to explore and research; (2) Technical Breakthrough, initially prompted by scientific curiosity, and later on by military and medical needs; (3) Commercial Development, driven by the market needs. Theoretical foundation of wireless power transfer technologies as known today dates back to 1819, when H. C. Oersted discovered that electric currents and magnetic fields are co-generated. In 1864, Ampere's Law, Biot-Savart Law and Faraday's Law were introduced into Maxwell's equations, thus characterizing the generation of magnetic and electric fields and their mutual effects. Later on, a unified study of electromagnetism was published in J. C. Maxwell's book *A Treatise on Electricity and Magnetism* [4], which set the theoretical foundations for WPT. In 1888, H.R. Hertz transmitted electricity over a small gap between two coupled coils using oscillator, being the first to experimentally confirm the existence of EM radiation. Nikola Tesla, the father of the AC electricity, has led the field and was the first to implement WPT based on microwave radiation. In 1896, he transferred a wireless signal over a 48 km distance. Later in 1899, 10^8 volts of high-frequency electrical power were transferred over 25 miles to light 200 bulbs and run an electric motor. The technology applied by Tesla had to be shelved as high voltages could result in electric arcs extremely hazardous to any human or electrical equipment nearby. The Wardenclyffe Tower was constructed in 1901 by Tesla, introducing the "Tesla Coil" to transfer electrical energy through the Ionosphere. The development was halted due to technical limitation (mainly low efficiency due to large-scale electric field). During the 1920s and 1930 the invention of magnetron enabled the conversion of

electricity into microwaves (thus laying the grounds for Microwave Power Transfer (MPT)). Wireless charging technology was abandoned until 1964, with the absence of technologies for converting microwaves back to electricity. In 1964, W. C. Brown implemented the conversion of microwaves to electricity successfully through a rectenna and demonstrated it by wirelessly powering a model helicopter. In 1975 Brown also beamed 30kW over 1-mile distance at 84% efficiency with Venus Site of JPLs Goldstone Facility. Though inductive coupling has been widely employed in the 1960's, no major breakthroughs were recorded. The recent progress in near-field coupling based power transfer, owes much to the portable electronics market, which grew in the 1990's. Research initially focused on the inductive power transfer systems, as they were an already well established technology. In the last few years, the capacitive coupling WPT systems present worthy alternative, by meeting the IPT systems both in efficiency and transmission distance, while potentially minimizing the hazardous effects both on humans and the surrounding[5].

1.3 Wireless Power Transfer Technologies:

A brief overview on wireless power transfer technologies is given in the following section. The section also discusses the fundamentals of the techniques employed as well as their advantages and shortcomings.

1.3.1 Acoustic Power Transfer:

Acoustic Power Transfer, also known as Acoustic Energy Transfer (AET), is a relatively new method for contactless energy transfer. While the common WPT systems (both coupling-based and RF) rely on EM field as the agent for energy transmission, the AET utilizes a pressured wave that propagates through a medium. A typical setup of an AET system is shown in Fig. 2. The system comprises the following: I. Transmitting transducer that converts electrical energy into a pressured wave; II. A medium through which the pressured wave propagates; III. A receiver transducer, usually followed by rectifier with capacitor in order to provide a DC output.

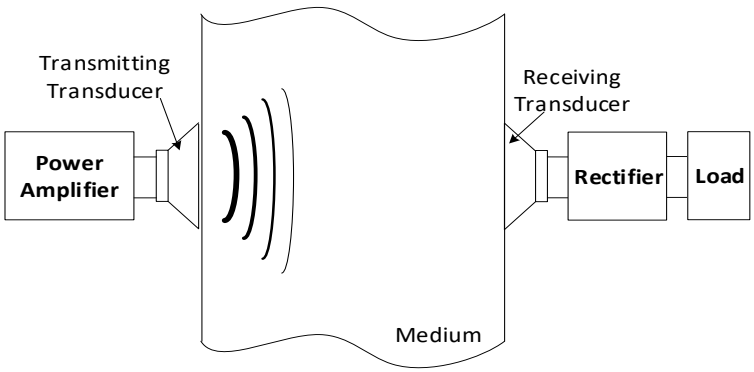

Fig. 2. An AET system consists of transmitting transducer that generates sound wave and a receiving transducer that converts the sound energy back to electrical

The transducers, in most cases, are built using piezo-electrical materials, as they are better suited for AET if they are well coupled to the medium[6]. The main advantage of AET systems over the conventional WPT is their ability to overcome metallic barriers, as the medium is quantified by the ability to propagate the pressured wave, meaning that hazardous environments (radiative or toxic e.g.) can be isolated in metallic tanks, and powered wirelessly without compromising the integrity of the isolation. Another common application of AET is Bio-Medical implants. The first use of AET dates back to 1985[7] when researchers powered implants by an external ultrasound source. In biomed applications the power consumption of the AET is typically under 100mW, with a top reported efficiency of 39.1% (at 29μW to 100mW)[8]. In through-wall applications the AET has reached 1kW, with 84% efficiency[9]. Although gaseous medium (air e.g.) for AET were investigated, the results presented were no more than proof of concept - 0.8mW were transferred over a distance of 30cm, with the best efficiency being 17% for an output power of 4μW. Bearing in mind that most standard applications feature an air-gap between the transmitter and receiver, the AET technology should probably remain an elegant solution for through-wall and biomed applications.

1.3.2 Laser Power Transfer:

Laser Power Transmission (LPT), or high intensity laser power beam (HILPB) is one of the most promising technologies for delivering power over long-range distances. The research has been mainly driven by the demand for powering unmanned aerial vehicles, as well as satellites and other remote mobile electrical consumers. A typical HILPB system consists of a high-power laser that converts electrical energy into a light beam at the transmitter, and a photovoltaic cell at the receiver that converts the EM radiation back to electrical energy. A schematic diagram of a HILPB system is shown in Fig. 3]. Key advantages for implementing LPT systems are: (1) The ability to effectively transmit energy over several km; (2) Potential to transfer several kW of power; (3) Compatibility with mobile applications, as the generated beam is highly directional. It is worth noting that LPT system are not restricted to large scale applications, as domestic applications for LPT charging has already been demonstrated by several companies.

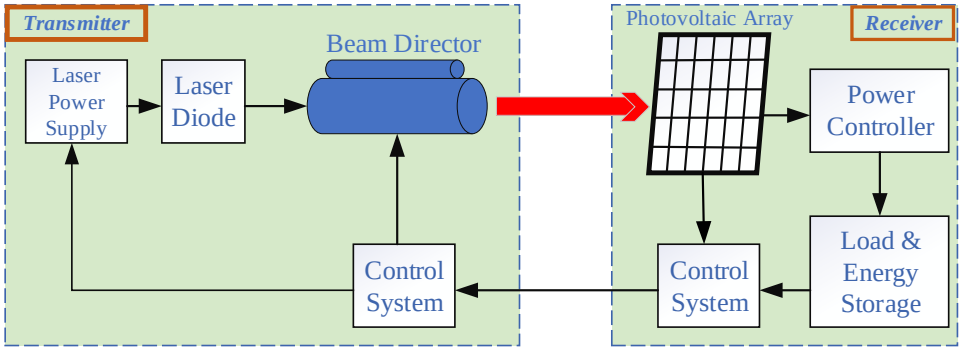

Fig. 3. Schematic diagram of a HILPB system

Two major shortcomings of LPT systems are their low efficiency (around 20% and below) and the need for a line-of-sight from the transmitter to the receiver. These disadvantages are likely to remain unsolved for the time being. The efficiency of both lasers and photovoltaics are limited to 50%. Therefore, without considering the losses incurred by other sources, the system efficiency is limited to 25%[10]. The line-of-sight prerequisite cannot be overcome by design. Another impeding factor is the radiative nature of LPT systems, which can be hazardous to humans or animals in the beam-path. In light of this, LPT applications would probably be restricted to applications that cannot be powered by alternative means (UAVs and satellites e.g.).

1.3.3 Microwave Power Transfer:

Microwave Power Transfer, or RF Power Transfer, delivers energy via microwave radiation from power stations to mobile devices wirelessly. The source(s) or Power Beacon(s) (PB) typically generates a signal in the 300MHz- 300GHz frequency range. The signal is received by a mobile device, in a similar way to wireless communication for data transmitting. Fig. 4(a) shows a schematic wireless powered communication network with separated energy access point (PB) and data access point. Fig. 4(b) shows wireless powered communication network with hybrid access point, thus providing both power and data. It should be noted that there are different alternatives for MPT, like transmitting power and data via the same channel simultaneously or transmitting power whilst the data transmission is idle[11].

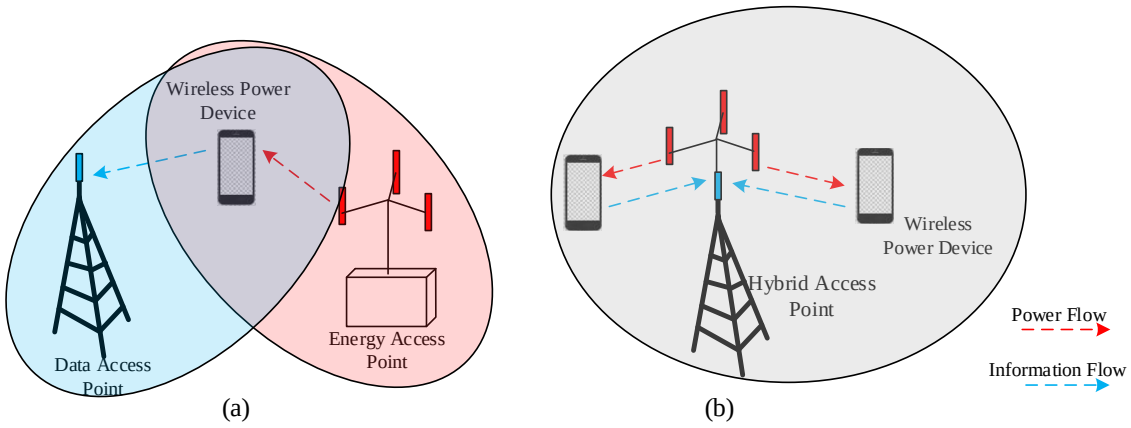

Fig. 4. (a) Wireless powered communication Network with separated energy access point and data access point; (b) Wireless powered communication Network with hybrid access point

The advantages of MPT include long effective transmission distance (up to several km), the potential to transfer several kW of energy, compatibility with mobile application and user convenience. Nonetheless, the MPT systems have a rather low implementation, primarily due to low efficiency (under 10% for high power applications) and high system complexity at both the transmitter and the receiver. Another constraining factor is the health issues involved in deploying high-power high-frequency radiative EM field near humans, thus focusing on

human-less applications such as UAV, or low-power low-distance applications such as powering mobile devices by WI-FI signal.

1.3.4 Inductive Power Transfer:

Inductive Power Transfer (IPT) systems separate to (1) Inductive Coupling; (2) Magnetic Resonance Coupling. Inductive coupling is based on energy exchange between two coils, by means of magnetic flux induction. The main difference between the two, is that in magnetic resonance coupling both the transmitter and the receiver are tuned to the same resonant frequency, hence creating strong coupling between the primary and the secondary. inductive coupling, however, relies on source-load proximity in order to establish high coupling.

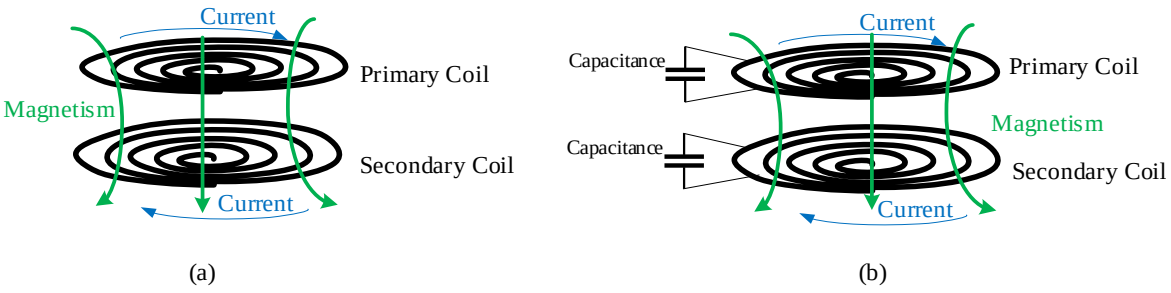

Fig. 5. (a) Inductive Coupling (b) Magnetic Resonance Coupling

The Magnetic Resonance coupling power transfer systems are prevalent in various fields, ranging from BioMed to EV. The main advantages that can be listed are high efficiency (above 90% at various papers, e.g.[12]–[16]) , high power transfer capabilities (several kW up to MW)[14], [17]–[22], good galvanic isolation, low system complexity and scalability. These advantages render IPT systems a preferable choice for near-field non-radiative energy transfer, as they can power a wide range of devices, from mW implants to kW EV. Possible disadvantages include limited transmission distance (from mm to m) and significant eddy current losses generated in near-by metals (limits application area). Considering the scope of this paper, it should be noted that despite its shortcomings, the IPT systems are the older and mature brother of the CPT systems discussed later. State-of-the-art designs that include regulation and tuning were presented at [23]–[30], indicating an ongoing interest in further development and deployment of IPT systems.

1.3.5 Scope of This Thesis:

The Thesis proposes a wireless current source, based on a capacitive power transfer system, with an adaptive matching network that is governed by a multi-loop mixed signal controller. Focusing on the compensation and control algorithm produces a broader solution for wireless transfer systems, both IPT and CPT.

2 Capacitive Power Transfer

Capacitive power transfer was first demonstrated by Nikola Tesla[31] in 1891, during a lecture at Columbia College. Notwithstanding its promising prospects, the method was almost completely forgotten until 2009, in part due to the commercial failure of this application in early years. The past ten years have witnessed a steady increase of research papers and commercial products related to CPT, promoting the CPT systems as a worthy competitor to the widespread IPT systems.

Capacitive power transfer systems operate in a similar way to the Inductive power transfer systems mentioned earlier, namely utilizing the electric fields that are developed between a pair (one or more) of coupling plates. The systems vary in their power stage, compensation networks, coupling interface and control mechanism, yet their basic structure and underlying principles of operation are somewhat identical. Common power stage, impedance matching networks and compensation methods are addressed in this chapter and provide an insight into the design trade-offs and considerations. The capacitive coupling structure is only addressed in a nutshell, as the work sets a broader focus on controlling the power stage and compensation networks.

2.1 Principle of Operation:

Placing two plates of conductor in proximity to each other with a dielectric placed between them forms a capacitor. The parallel plates capacitance is given by:

$$C = \frac{\varepsilon A}{d} \tag{2.1}$$

where ε is the dielectric constant, A the plates overlapping surface area, and d is the distances between the plates. In case sinusoidal voltage V is applied on the capacitor plates, sinusoidal current flows through it, such that (phasor representation):

$$I_c = j\omega CV \tag{2.2}$$

implying that for a given capacitor, the higher the frequency or/ and the voltage, the higher the current would be. Eqs. (2.1) and (2.2) constitute the cornerstones of capacitive power transfer, as they embody the physical essence of the system by setting the coupling formation and the sinusoidal voltages required for power transfer. Hence, the CPT may be envisioned as a power converter that contains a series capacitor(s) separating the source and load. Typical structure of a CPT system consists of a DC source, high frequency inverter and a compensation network at the transmitter, as well as a compensation network, a rectifier and load at the receiver, as shown at Fig. 6.

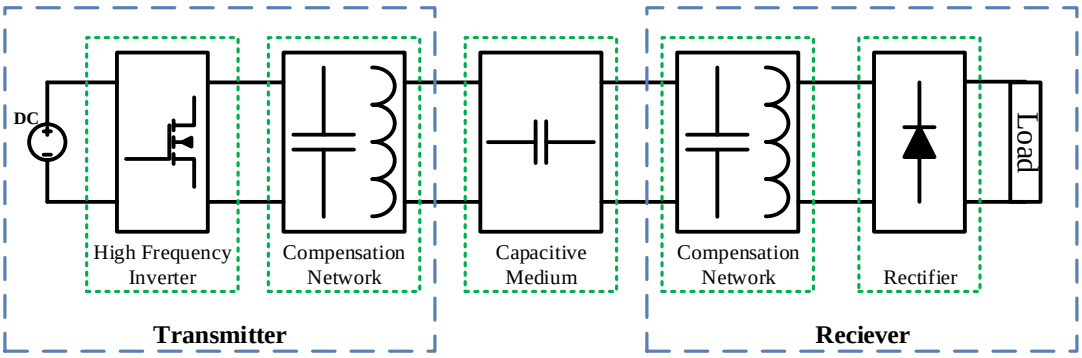

Fig. 6. Typical Structure of CPT system

2.2 Capacitive Interface:

The capacitive interface was thoroughly investigated in[32]–[35]. However, as this work is thematically confined to control, the coupling interface shall follow the topologies shown in Fig. 7.

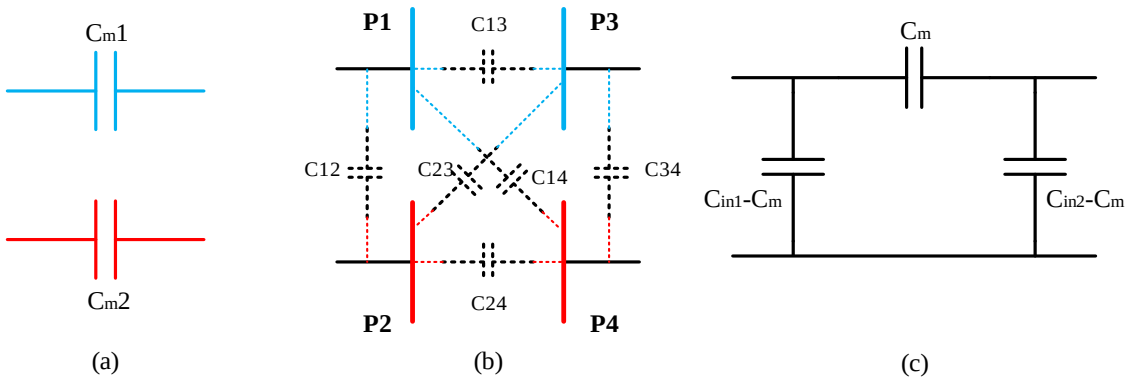

Fig. 7. (a) Capacitive Coupling Plates; (b) Total Capacitance Model; (c) Capacitor Pi-Network model

Placing two pairs of conducting plates that face each other as shown in Fig. 7(a), results in an all-inclusive configuration of six effective capacitors, as shown in Fig. 7(b). In order to alleviate heavy calculations, the network in 7(b) is usually transformed into capacitive PI network, as shown in Fig. 7(c). According to [32]:

$$C_{in1} = C_{12} + \frac{(C_{13}+C_{14})(C_{23}+C_{24})}{C_{13}+C_{14}+C_{23}+C_{24}} \tag{2.3}$$

$$C_{in2} = C_{34} + \frac{(C_{13}+C_{23})(C_{14}+C_{24})}{C_{13}+C_{14}+C_{23}+C_{24}} \tag{2.4}$$

$$C_M = \frac{C_{24}C_{13}-C_{14}C_{23}}{C_{13}+C_{14}+C_{23}+C_{24}} \tag{2.5}$$

In resonant CPT systems, the parallel capacitors are mostly part of the resonant tank, therefore affecting the resonant frequency, and is usually compensated by a much larger parallel capacitors to maintain constant resonant frequency.

2.3 Power Stage Analysis:

As shown in Fig. 6 and discussed earlier, a high frequency inverter (Power Stage) is a mandatory part of any CPT topology. The choice of the power stage is subject to cost, size, coupling capacitance, voltages/ currents, etc. The aim of the power stage to create a square-wave input voltage signal into the compensation network. Assuming that the compensation network has a high enough Q, the square-wave voltage may be treated under First Harmonic Approximation (FHA), as sinusoidal wave of the drive frequency. With these design considerations, in addition to the fact that resonant work-mode is the widespread approach, Full-Bridge and Half-Bridge inverters are the preferred candidates, although other configurations are available as well. It's important to note that CPT systems can operate in an un-resonant mode, like in most single switch CPT converters.

2.3.1 Single Switch Power Stage:

There are several types of basic single active switch converters: 1) Buck; 2) Boost; 3) Buck-Boost; 4) SEPIC; 5) Cuk; 6) Zeta[36]. In particular, Cuk, Zeta and SEPIC have a series capacitor, permitting the superficial yet practical division of the converter into a "transmitter" and a "receiver". While in Buck-Boost converter the inductor can be divided into two inductors separated by coupling capacitors. The standard topologies and their modification for CPT systems is shown in Fig. 8. It can be readily observed that the modification needed to reconcile the converters with a CPT system is minor. Hence, most of the analysis and control mechanisms may still be relevant for the modified topologies. Unlike Half-Bridge and Full-Bridge, the single switch topologies are inapplicable to any compensation network, and is therefore presented as a complete system.

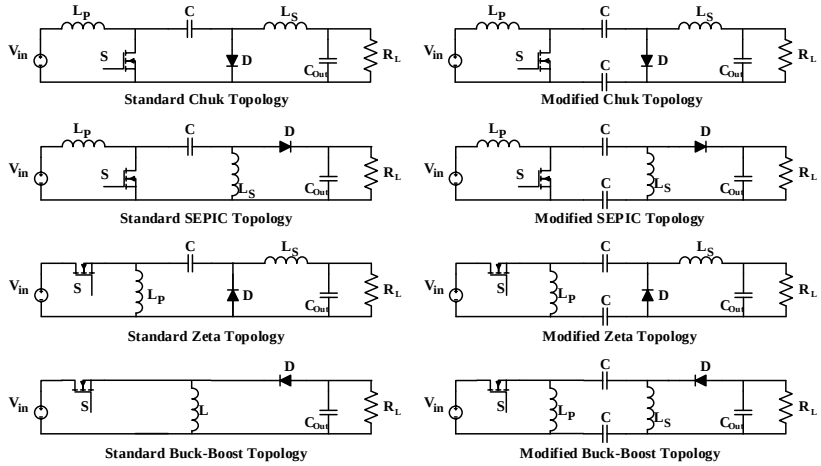

Fig. 8. Standard DC-DC Topologies and their modification for CPT systems

The topologies shown in Fig. 8 usually do not operate in a resonant mode, hence, don't significantly amplify the voltage across the coupling capacitors, with respects to the input voltage. According to [36], in order to transfer high current to the load, high frequency or high

coupling capacitance or both are needed. Coupling capacitance, which in practical conditions may vary, dramatically decreasing the power transferred. Regardless of these drawbacks, >1kW CPT systems were presented in [36], [37], with efficiency above 92%. A typical implementation of such topologies is for fixed conditions, where the coupling capacitance is constant.

2.3.2 Half- Bridge Inverter:

Half-Bridge inverter is a popular choice for resonant circuits' power stage, as an effective AC excitation method. It usually consists of two MOSFET or GaN switches, driven by PWM signal. Fig. 9 shows Half-Bridge power stage configuration. As most CPT system operate under resonant or quasi-resonant conditions (50% duty cycle), a series capacitor (C_{dc}) is connected to the switching node, therefore blocking the DC component of the input signal and delivering to V_y pure sinusoidal harmonics. Once the AC signal is generated, it can be applied to any kind of resonant tank (various resonant tanks discussed later in this chapter), both for IPT and CPT systems[38].

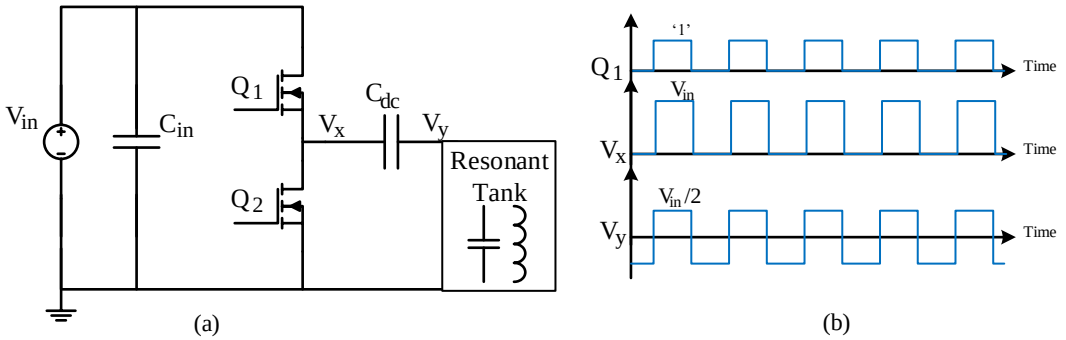

Fig. 9. (a) Half-Bridge power stage with DC capacitor; (b) Typical Wave-forms

Another practical advantage is a single ground node (unlike Full-Bridge), which potentially simplifies the sensing circuitry. This design is usually addressed as asymmetrical Bridge inverter in the literature. The symmetric topology splits the C_{ds} capacitor into two capacitors, similar to a Full-Bridge where $Q_{2,3}$ is replaced with capacitors.

2.3.3 Full- Bridge Inverter:

The Full-Bridge (FB) inverter is probably the most robust power stage option for effective AC excitation. It usually consists of 4 MOSFET or GaN transistors that are driven by PWM signal, as shown in Fig. 10(a). The Full-Bridge topology - at 50% duty cycle drive - creates $\pm V_{in}$ square wave at V_x (Fig. 10(b)), and it lacks the DC component by design. Therefore, any resonant tank can be connected to the inverter's output. The FB also minimizes the stress over of the switches, as the same power flows through a greater number of switches.

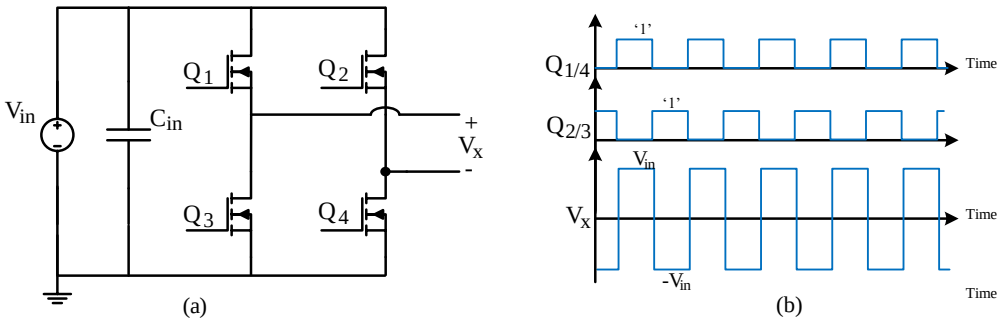

Fig. 10. (a) Full-Bridge power stage; (b) Typical Wave-forms

Though in terms signal generation and power transfer the FB presents notable advantages, the sensing circuitry faces a challenge, as there is no common ground level. In case of a bi-directional CPT, the FB can also be active rectifier, thus, the receiver and the transmitter power stages are mirrors image of one another.

2.4 Compensation Networks Analysis:

In most CPT systems that operate in the few mm to tens of cm range, the coupling capacitance is in the pF range. With such low capacitance, the impedance of the coupling capacitance is in the tens to hundreds [kΩ], assuming a switching frequency of 0.5- 10MHz. To circumvent the series connected high impedance component, one would either increase the switching frequency, or the voltage across the coupling medium. An alternative approach is to create a state where the medium impedance is not higher than the other components', thus making it a preferable path for energy flow (or a combination between the options). Resonant tanks (or impedance matching networks) are a natural solution for those requirements. Moreover, the impedance matching networks can minimize the switching losses (Zero Voltage Switching (ZVS) or Zero Current Switching (ZCS)) and minimize the system's overall size. Since any combination of reactive components creates a resonant tank, which can get very exotic and complex while being characterized by multiple resonant frequencies, this work covers the most common compensation topologies.

2.4.1 Series Compensation (L):

Series compensation, which utilizes the coupling capacitor as the resonant capacitor, was extensively used in the early CPT systems [39], [40]. Fig. 11 shows the circuit topology of series *L* compensator, with a single or split inductor. In case of series resonant, the inductance can be either a single inductor, or being separated into primary and secondary windings without affecting the system's behavior.

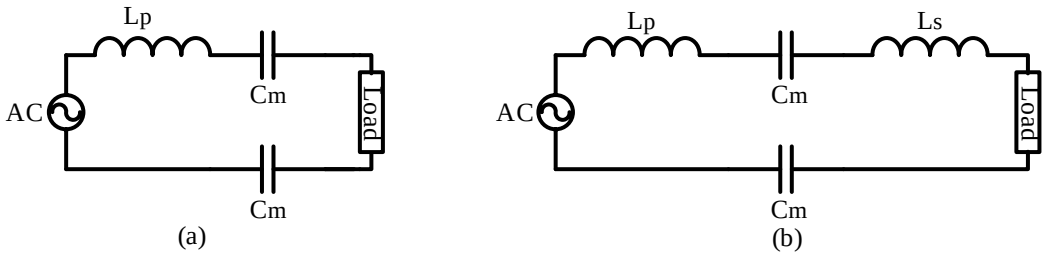

Fig. 11. Series L compensator. (a) Single Inductor; (b) Split Inductor

The inductance value and the resonance frequency are coupling-capacitance dependent. In order to minimize the overall system volume, small, low inductance coils may be applied to drive the resonant frequency very high. In a practical implementation, the split inductor is replaced with a single coil at the transmitter side, reducing the receiver's complexity and size. In addition, the single coil configuration provides better EMI suppression at the primary side.

The advantage of this topology lies in its simplicity and versatility. It is applicable for low and high-power setups, from miniature medical implants to DC machines that operate at tens of kilo-hertz (mostly for high coupling capacitance and high-power applications), or at hundreds of mega-hertz (low capacitance-low power applications). At nominal operating conditions:

$$V_{out} = V_{in} \tag{2.6}$$

$$P_{out} = \frac{V_{in}^2}{R_L} \tag{2.7}$$

The main disadvantages of series L compensator are its sensitivity to coupling capacitance variation, and the trade-off of inductor's size vs. switching frequency. The inductance is proportional to:

$$L_1, L_2 \approx \frac{1}{\omega^2 C_m} \tag{2.8}$$

The series resonance utilizes the coupling capacitance as the resonant capacitor, which may vary in practical implementation. In such systems, if unregulated, a slight change in C_m drops the power transferred capabilities drastically.

2.4.2 LC Compensation:

In most CPT applications the low coupling capacitance challenges the system's ability to meet the power demand. In order to increase the equivalent coupling capacitance, parallel capacitors C_{ex1}, C_{ex2} can be connected to the coupling interface, resulting in a double-sided LC compensation circuit, as shown in Fig. 12.

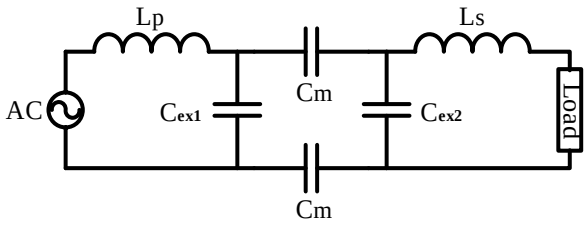

Fig. 12. Double-Sided LC Compensation

For this compensator usually C_{ex1}, C_{ex2} >>C_m, thus, the effective capacitance increases drastically. Similar to IPT systems, capacitive coupling coefficient k_c normalizes the ratio between the self and external capacitance, according to:

$$k_c = \frac{C_m}{\sqrt{C_1 C_2}} \tag{2.9}$$

where C_m is the mutual capacitance, and C_1, $C_2 = C_{ex} + C_{in}$, are the total capacitance as seen from the source/ load. The increase in capacitance lowers the requirements of inductance, decreasing L_P, L_S in size and volume. As the parallel capacitance is predominant, L_P, L_S resonate with the equivalent capacitance that it sees (primarily with C_1, C_2, respectively).

$$L_P, L_S \approx \frac{k_c}{\omega^2 C_m} \approx \frac{1}{\omega^2 \sqrt{C_1 C_2}} \tag{2.10}$$

For C_{ex1}, C_{ex2} >>C_m the resonant frequency is C_m independent, therefore maintaining resonance under misalignment and distance variation condition. This advantage is usually made use of in high power or long-distance applications. Under nominal conditions, the output power is:

$$P_{out} = \left(\omega V_{in} \frac{C_1 C_2}{C_m}\right)^2 R_L \tag{2.11}$$

According to $P_{out} = \left(\omega V_{in} \frac{C_1 C_2}{C_m}\right)^2 R_L$ (2.11) the power is inversely proportional to the coupling capacitance. The system power increase with increase in distance, though the efficiency drops aggressively. Further LC compensation analysis, and its current source behavior as addressed in chapter 3 in the form of double-sided LC topology, was in the focus of this work.

2.4.3 LCL Compensation:

Combining L and LC compensators results in a double sided LCL topology as shown in Fig. 13. Double-Sided LCL Compensation. The additional inductors L_{s1}, L_{s2} can partially or fully compensate for C_m dependent on the work mode. The major disadvantages of double-sided LCL are is size and volume of L_{s1}, L_{s2} as the coupling capacitance is low, and the power vs C_m are still in inverse relation. As the disadvantages of both topologies remained unsolved to date, LCL compensator are rarely used [34].

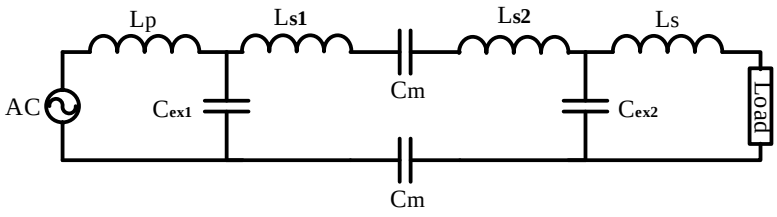

Fig. 13. Double-Sided LCL Compensation

2.4.4 LCLC Compensation:

One possible solution to the L, LC, LCL shortcomings is the double-sided LCLC compensation, as shown in Fig. 14. Double-Sided LCLC compensator.

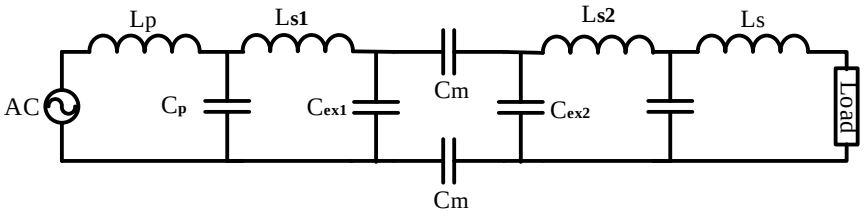

Fig. 14. Double-Sided LCLC compensator

This multi-resonant configuration enables various work-modes. For instance, L_p, C_p can be thought of as a current source, while the L_{s1}, C_1 amplify the voltage for effective power transfer. Another advantage is the proportional relation with the coupling capacitance. Under nominal operating conditions [33]:

$$P_{out} = \left(\omega C_m \frac{C_p C_s}{C_1 C_2} V_{in}\right)^2 R_L \tag{2.12}$$

The P_{out} can also be regulated, independent of C_m by the passive components' values. The main disadvantage of double-sided LCLC is the complexity and overall size, weight and cost. For optimal power transfer conditions, the reactive components ratios and values must be carefully chosen and be as steady as possible. In practical implementation it's extremely complex to fulfill these requirements as the effective value of such components is dependent on factors such as currents, voltages, temperature and parasitics.

2.5 Active Compensation Methods:

The previous section discussed reactive components network compensation as a mean to maximize and optimize the power transfer capabilities over the capacitive medium. Yet, none of the topologies can maintain constant output voltage or current under varying C_m scenario, as can easily be seen in the P_{out} functions. Constant output current or voltage can be achieved by means of active compensation methods, as discussed in this section. It is important to realize that the following compensators do not necessarily increase the efficiency or maintain optimal work modes such as resonance or soft-switching.

2.5.1 Frequency Control:

Assuming the presence of resonant tanks at the transmitter and receiver, the I_{out}/V_{in} or V_{out}/V_{in} transfer function typically assumes the curve shapes shown in Fig. 15. For this type of control mechanism, the switching frequency is usually above the resonant frequency to minimize switching losses and simulate current source behavior at the transmitter.

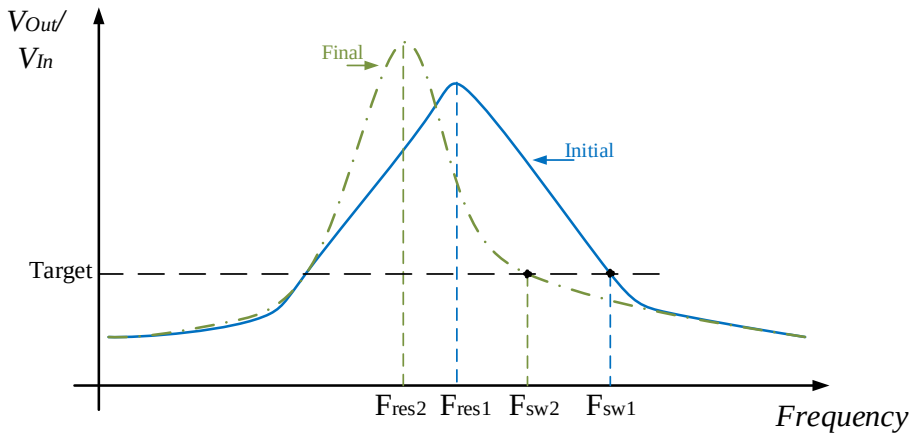

Fig. 15. Typical Resonant Tank Transfer Function

Under varying C_m conditions, the transfer function changes accordingly. Assuming that under new C_m value the target output power is below its peak point, the switching frequency can be changed from F_{sw1} to F_{sw2}, delivering the target output, as shown in Fig. 15. The advantages of the frequency compensation are its simplicity and compatibility with almost any kind of resonant tank. As this method is applied in various resonant and quasi-resonant systems [41], [42], controller design and analysis are easy to come by. The disadvantages of the frequency control are potentially low efficiency due to un-resonant drive, and varying frequency which can be problematic in sensitive systems where the power stage frequencies have to be filtered out.

2.5.2 Active Variable Reactance:

Active Variable Reactance (AVR) method, or the wide-spread AVR rectifier are in some way the impedance equivalent of switched-mode converters. The operating principle of the AVR is to create several power routes with different impedances, then to periodically change the routes, thus presenting equal average impedance, in an analogy to Buck converter. Usually the AVR incorporates an inductor and capacitor with impedance of $+jX$ and $-jX$ accordingly. The current can flow either through the inductor, the capacitor, or in both components, subject to the compensation type.

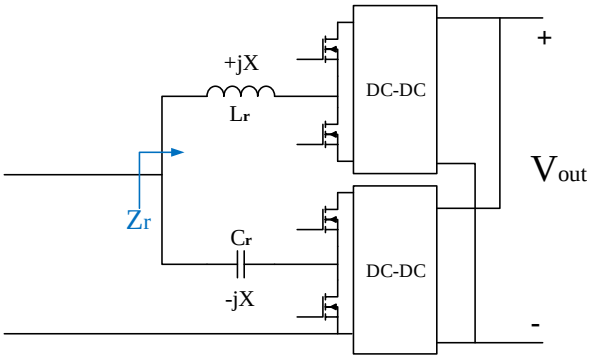

Fig. 16. AVR rectifier with DC-DC converters

Fig. 16 shows one possible implementation of the AVR rectifier [43]. The main advantage of the AVR is the ability to attain any impedance in the $-jX \div +jX$ range. The disadvantages can be readily inferred from Fig. 16; its overall size, the component count and system complexity, superimposed with a reduced efficiency as the AVR has its own losses. Nevertheless, it enables continuous compensation for medium variations while maintaining constant work frequency and output power (up to system limits). Usually implemented at the receiver side, it acts both as a rectifier and impedance compensator.

2.5.3 Virtual Impedance:

The virtual impedance compensation is an elegant method for simulating reactive components in a circuit, while controlling their effective impedance [44]. The control mechanism receives an input of the target behavior of the system, e.g. for resonant circuit. The input can be a sinusoidal wave of a desired frequency and amplitude (or their representation). Then, using measurements of voltages/ currents of the system, the input voltage and the power stage switching are set in such a way that the voltage/current acts as if a capacitor or an inductor are placed instead. The advantage of applying the virtual impedance compensation is the ability to simulate an impedance of almost any value, at zero volume and weight (compared to AVR e.g.). Its main disadvantages are the need for varying voltage source, the imposed and practically inevitable switching conditions at the power stage, and the need for sensing circuitry and controller complexity.

2.5.4 Tunable Components:

Unlike traditional cord-based power transfer systems, where the variation parameter is usually the system's load, in wireless system both the load and the medium can vary. In case of medium variation, the overall system behavior can considerably depart from normal, changing the resonance frequency, gain, efficiency et al. However, the transfer function curves are the combination of C_m and other reactive elements (resonant tank e.g.). Therefore, any variation in C_m can be compensated by changing the effective impedance of other component(s). In gyrator systems, where $I_{out}=GV_{in}$ and vise-versa, $G=f(C_m, L, C)$, initial value of G can be achieved by

tuning *L-C*, to the desired value. Unlike other methods, the tunable capacitor or inductor does not average its value over several switches or emulates the components operation - which usually trades off with efficiency or complexity - but rather shapes the system transfer curves in keeping with the goal behavior: constant frequency, constant power, high efficiency or any other. In this work, a variable inductor is presented as an adaptive compensator and analyzed in the next chapters.

3 Closed Loop Tuning of a Double-Sided LC Capacitive Power Transfer System:

The following chapter presents the operation of a resonant double-sided LC capacitive wireless power transfer system, controlled by an adaptive multi-loop controller. In order to fully understand the system's behavior, a step by step analysis is carried out to clarify the method with a rudimentary circuit up to a full implementation in integrated setups. From this chapter on, the transmitter and the receiver shall be addressed as a primary and secondary, respectively. It should be emphasized that the control guidelines presented henceforth can be applied to different power stage topologies/ resonant tank structures as long as the guidelines are followed.

3.1 Double Sided LC Matching Network:

The system described is a resonant DC-DC converter that is activated by a multi-loop mixed-signal controller. The power stage consists of a full- bridge inverter on the primary side, followed by a LC impedance matching network on both the primary and secondary sides (mirrored), and the load is fed via a diode rectifier. The capacitive interface is established by two pairs of metal plates. The simplified schematic of the double-sided LC resonant WPT is depicted in Fig. 17.

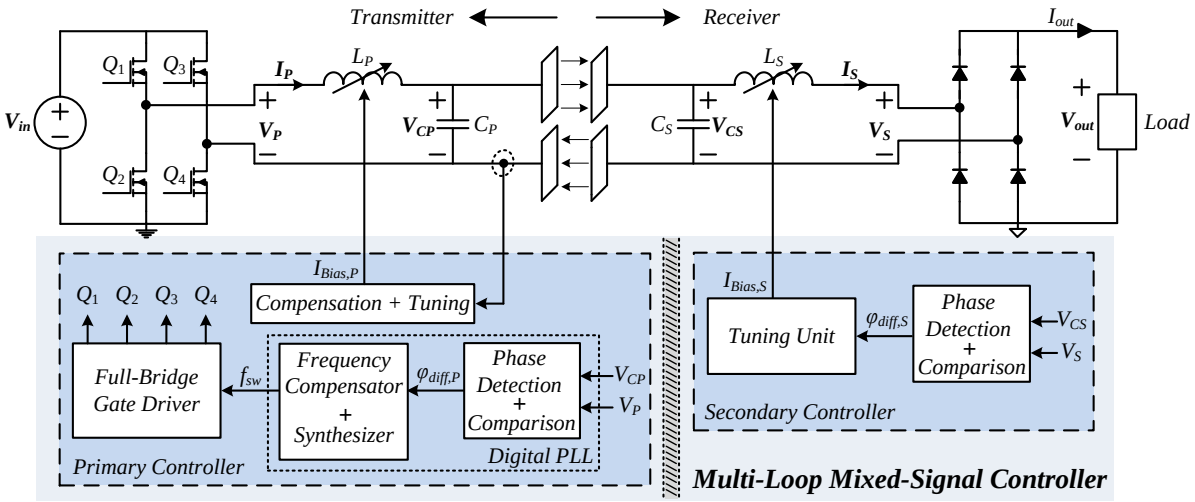

Fig. 17. Simplified schematic diagram of a double-sided LC capacitive WPT system with an adaptive multi-loop controller

3.1.1 Static Model:

The system behavioral analysis starts with a simplification of the circuit in Fig. 17. Disregarding the non-linear components (switches and diodes) enables the analysis of the frequency response of the circuit. Under the first harmonic approximation, the full-bridge inverter, operating at 50% duty cycle, can be addressed as a single harmonic sinusoidal voltage source, with frequency of f_{drive} and peak amplitude of

$$V_p = \frac{4}{\pi} V_{in} \tag{3.1}$$

Provided that the load consists of a resistor with a parallel capacitor and is driven by an AC current source (as explained in the next section), it can - according to Steigerwald [45] - be replaced with:

$$R_{ac} = \frac{8}{\pi^2} R_{Load} \tag{3.2}$$

in terms of power consumption, or simply R. Based on these two assumptions, an equivalent circuit to that in Fig.17 is given in Fig. 18. $Z_{1\text{-}4}$ are the impedance at each point of observation:

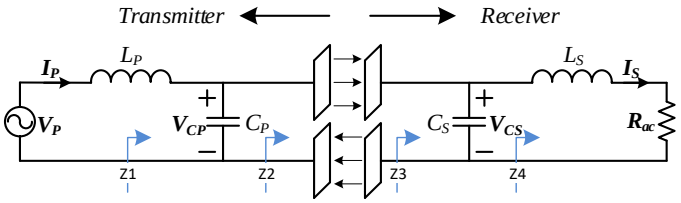

Fig. 18. Simplified Circuit; $Z_{1\text{-}4}$ Impedance at observation points accordingly

$$Z_4 = R_{ac} + sL_s \tag{3.3}$$

$$Z_3 = Z_4 || \frac{1}{sC_s} = \frac{R_{ac}+sL_s}{s^2C_sL_s+sC_sR_{ac}+1} \tag{3.4}$$

$$Z_2 = Z_3 + \frac{2}{sC_m} = \frac{s^2L_s(2C_s+C_m)+sR_{ac}(2C_s+C_m)+2}{sC_m(s^2C_sL_s+sC_sR_{ac}+1)} \tag{3.5}$$

$$Z_1 = Z_2 || \frac{1}{sC_p} \tag{3.6}$$

$$Z_{in} = Z_1 + sL_p \tag{3.7}$$

$$I_p = \frac{V_p}{Z_{in}} \tag{3.8}$$

$$V_{cp} = \frac{V_p Z_1}{Z_1+sL_p} \tag{3.9}$$

$$V_{cs} = \frac{V_{cp} Z_3}{Z_3+\frac{2}{sC_m}} \tag{3.10}$$

$$V_{out} = \frac{V_{cs} R_{ac}}{R_{ac}+sL_s} \tag{3.11}$$

$$I_s = \frac{V_{cs}}{R_{ac}+sL_s} \tag{3.12}$$

Bearing in mind that the self-capacitances and the mutual coupling capacitance C_m of the coupling interface are lower than the total parallel capacitances C_P and C_S [33] (meaning that the change of C_m wouldn't affect C_P C_S significantly), and that the drive frequency is near the matching networks' resonant frequency (i.e., $f_0 = \sqrt{L_P C_P}$), V_{out}/V_{in} expression can be written as:

$$\frac{V_{out}}{V_{in}} = \frac{Z_1}{Z_1+sL_p}\frac{sC_mZ_3}{1+sC_mZ_3}\frac{R_{ac}}{R_{ac}+sL_s} \tag{3.13}$$

While eq.(3.5) does not contribute an intuitive insight in the system planning level, one does see the considerable number of parameters that affect the load voltage/current. Fig. 19 plots V_{out}/V_{in} transfer curves for 3 of inductor/capacitor couples around the same resonant frequency.

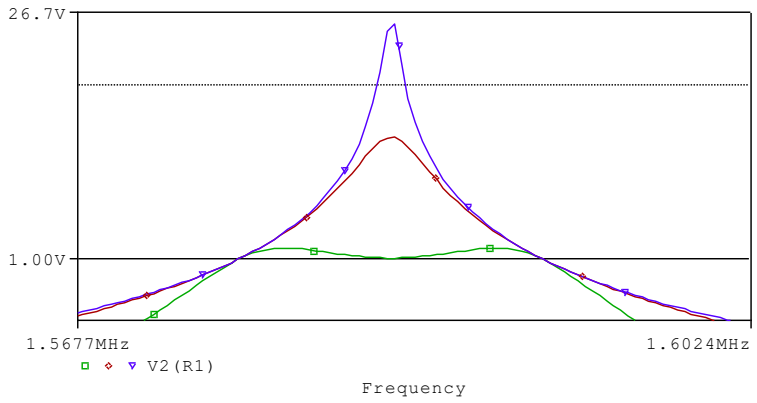

Fig. 19. Vout/Vin (example)

This non-linear frequency response can prove problematic in terms of compensator design, as even a minor change in any parameter (Drive frequency, load, passive components, temperature etc.), may result in a drastic change of energy transfer to the load, thus, limiting the system to a fixed working point (for each custom design). An alternative approach is to regard the system as a voltage controlled current source, or, gyrator.

3.1.2 Double Sided LC CPT as a Current Source:

Further analysis of the circuit at Fig. 18 should facilitate its understanding. Replacing the coupling interface secondary impedance matching network and load with an equivalent impedance Z_2, reveals a well-known topology: A series resonant converter with parallel loading, as shown in Fig. 20.

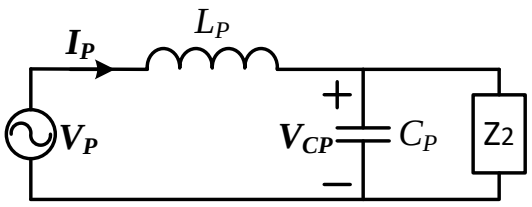

Fig. 20. Transmitter equivalent circuit. A series resonant converter with parallel loading

For this circuit, and under resonant drive conditions, the quality factor Q is:

$$Q = \frac{Z_2}{Z_r} = \frac{Z_2}{2\sqrt{\frac{L_p}{C_p}}} = \frac{V_{cp}}{V_p} \tag{3.14}$$

which implies that the output voltage is a function of the load and the resonance tank, in a similar fashion to static analysis. Furthermore, applying Norton's theorem to the circuit in Fig. 20, transforms the latter to a parallel resonant circuit that is driven by current source, as shown in Fig. 21.

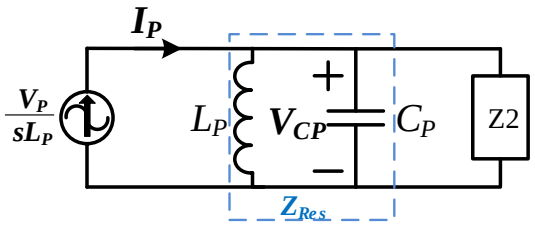

Fig. 21. Equivalent simplified circuit

The impedance denoted Z_{Res} is formed by the parallel connection of the elements encircled in Fig. 21:

$$Z_{Res} = sL_p \,||\, \frac{1}{sC_p} = \frac{sL_p}{1+s^2L_pC_p} \tag{3.15}$$

For $f_0 = (2\pi\sqrt{L_PC_P})^{-1}$, Z_{Res} diverges, therefore acts as a current source independent of Z_2 impedance. Although the current flows through Z_2, the plate structure sets that the same current in the secondary, where it traverses the receiver's resonant tank.

Having clarified the current source behavior, further analysis of the system as a gyrator can be carried out. Fig. 22 presents the circuit for analysis. Switching the load with a voltage source allows the individual examination of the independent sources in the setup.

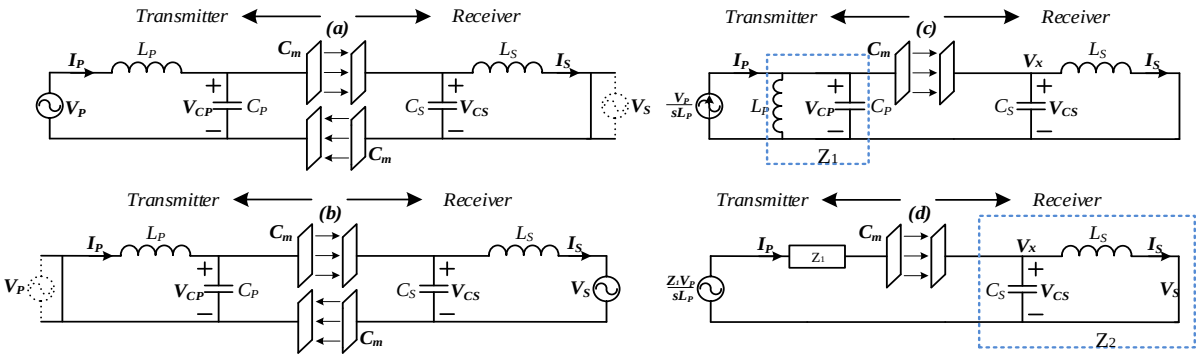

Fig. 22. Gyrator analysis circuit; (a) V_s=0; (b) V_p=0

As shown in chapter 2, the capacitive interface Fig. 22 (a), (b) can be transformed into a single capacitor with a capacitance equal to the series capacitance connection of the original capacitors. Applying Norton's Theorem should take the reader from Fig. 22 (a) to Fig. 22 (c). The

following equations extract I_s. For $\omega_0 = (\sqrt{L_P C_P})^{-1} = (\sqrt{L_s C_s})^{-1}$ and $Z_1 = L_p \| (C_1 - C_m) = Z_2 = L_s \| (C_2 - C_m) = j/\omega C_m$.

$$V_x = V_{in} \frac{Z_2}{Z_1 + \frac{1}{j\omega C_m} + Z_2} = V_{in} \frac{Z_2 j\omega C_m}{1 + (Z_1 + Z_2) j\omega C_m} = \frac{V_p Z_1 Z_2 j\omega C_m}{(1 + (Z_1 + Z_2) j\omega C_m) j\omega L_p} \tag{3.16}$$

$$I_s = \frac{V_x}{j\omega L_s} = \frac{V_p Z_1 Z_2 j\omega C_m}{(1 + (Z_1 + Z_2) j\omega C_m) j\omega L_p} \frac{1}{j\omega L_s} \tag{3.17}$$

Inserting Z_1, Z_2 under resonance conditions into eq. (3.17) produces:

$$I_s = \frac{-jV_p C_1}{\omega L_s C_m} = \frac{-jC_1 C_2 \omega_0}{C_m} V_P \tag{3.18}$$

The symmetry of the system means that under the same assumptions and analysis, the input current is:

$$I_P = \frac{-jV_s C_2}{\omega L_p C_m} = \frac{-jC_1 C_2 \omega_0}{C_m} V_S \tag{3.19}$$

The results of eq.(3.18),eq.(3.19) are in keeping with the results of [46] which show that the output current depends on the input voltage, and the input current depends on the output voltage. In other words, the circuit is a gyrator with a gyration constant of

$$G = \frac{-jC_1 C_2 w_0}{C_m} \tag{3.20}$$

The above behavior is encouraging with respect to WPT systems as it effectively establishes a wireless current source. The simplified behavioral model presented in Fig. 23 is the essence of the system's goal functionality.

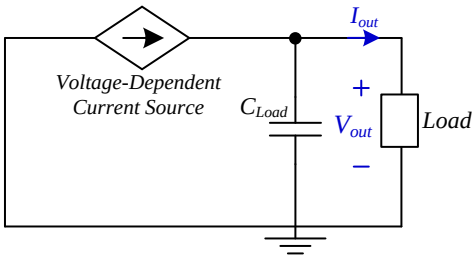

Fig. 23. Simplified behavioral model for the output side of the CPT system

Furthermore, eq.(3.13), eq.(3.19), yield the same results (under the same conditions), while the structure of eq.(3.19) unveils a more graspable approach to control the output current. Note that the current source - while uncontrolled - can deliver the desired current only under static conditions. Any variation of components or drive frequency should break the gyration relation and lead to a current drop.

3.1.3 Medium Variation Effects:

With the static behavior of the circuit in mind, it is imperative to investigate the medium variation effect on the system. As in any wireless power transfer system, the coupling between the transmitter and the receiver plays a key factor. The coupling may vary as a function of the conducting sheets size as well as their distance and orientation. These effects on C_m were broadly discussed in [32]–[35]. In our work, however, C_m is treated as an equivalent coupling capacitance, irrespective of the variations discussed. As eq. (3.19) has a non-linear behavior with respect to C_m, it is altogether better to gain insight into the problem visually. To this end, PSPICE simulation of a circuit in Fig. 18 is performed with the following parameters: $L_P=L_S=30\mu H$, $C_P=C_S=500pF$, $R_{Load}=50\Omega$. Fig. 24 illustrates the effect of C_m on the output current (with all other components are fixed).

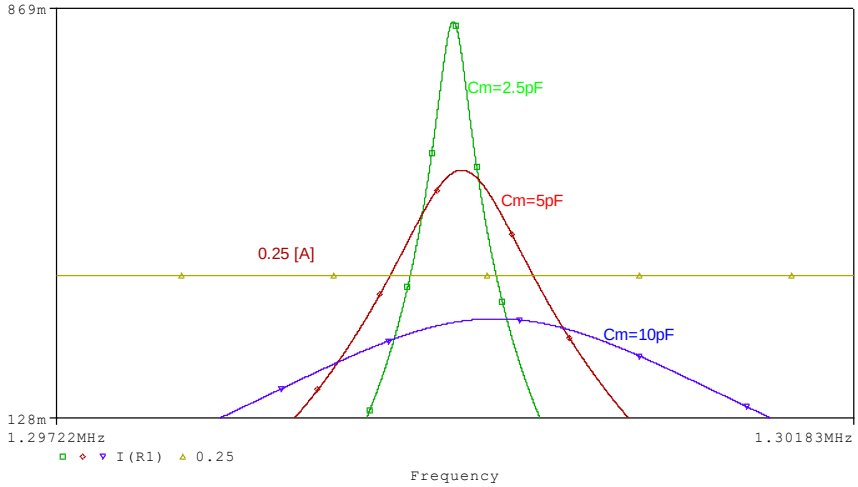

Fig. 24. DS_LC Iout, Green- Cm=2.5pF, Red- Cm=5pF, Blue- Cm=10Pf; LP=LS=30uH, CP=CS=500pF, RLoad=50Ω

Consistent with the task of creating a current source, each C_m curve should intersect the target current marker (i.e., the 0.25[A] yellow line in Fig. 24) at some point. The Cm curves can be readily distinguished by the following parameters :(1) Amplitude of the peak current; (2) Frequency of peak current. One immediate observation from Fig. 24 is the inability to compensate for all medium changes by changing the drive frequency f_0. This fact confines the effective control into a very narrow range of C_m variations. From eq. (3.19), the magnitude of I_S is a function of V_P, and the passive components (C_P, L_P, C_S, L_S). Whereas controlling V_P seems a trivial solution to the problem, its implementation requires an additional DC-DC converter with a wide range of output voltages (as can be seen in Fig. 24), which in effect lowers the efficiency and complicates the overall system design. Maintaining constant output current by means of passive component is called for, as the parameters V_P and f_0 has limited capacity to solve the task at hand. Converting ω_0 to $\omega_0 = (\sqrt{L_P C_P})^{-1} = (\sqrt{L_S C_S})^{-1}$ in eq.(3.19) results in eq.(3.21). Eq. (3.21) proposes an alternative way for solving the task at hand:

$$I_s = \frac{-jC_p\sqrt{C_s}}{C_m\sqrt{L_s}}V_P \tag{3.21}$$

The above expression encapsulates the solution to maintaining a constant current under varying C_m conditions, as it holds that compensation is achieved through changing the inductance or capacitance (or both). While varying capacitors and inductors offers additional degree of freedom for the compensation mechanism, this work covers the case of variable inductor exclusively, backed up earlier experimentally. To demonstrate, we repeat the simulation in Fig. 24, but with inductors L_P=L_S=20μH. Fig. 25 shows that for the new inductance, all traces intersect the load line at the some point. In comparison with Fig. 24, Fig. 25 shows different peak current amplitude at different frequencies, indicating that changing the passive components must involve frequency sweep as well. These two insights are fundamental for the following control algorithm and controller operation. In terms of the transfer function, an adjustment of the current transfer curve must be applied, provided that the peak point meets the set target. Another helpful observation is the inductor's voltage phase shift. Fig. 26 shows that for any C_m the peak of the output current is at the same frequency as a 90deg phase shift.

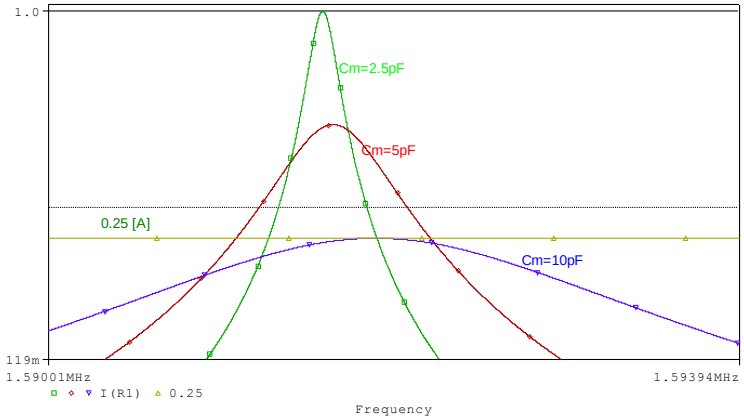

Fig. 25. DS_LC Iout, Green- Cm=2.5pF, Red- Cm=5pF, Blue- Cm=10Pf; LP=LS=20uH, CP=CS=500pF, RLoad=50Ω

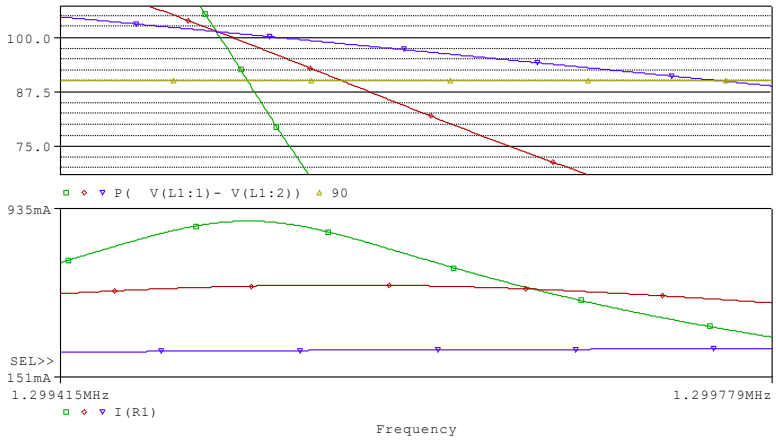

Fig. 26. Voltage phase shift of Lp+ - Lp-

3.2 Controller Operation:

The analysis and observations given thus far has set the ground for adaptive controller that monitors, tunes, and enables steady and constant current to the receiving side. In essence, the controller has two tasks: (1) To locate the peak current frequency (the resonant frequency); (2) To adjust the impedance matching network to correspond peak and target currents. The overall current regulation is facilitated by three control loops, as shown in Fig. 17. Two loops are at the primary, while the third loop is located at the secondary circuit. The control loops are distinguished by their control objectives and bandwidth requirements, such that the operating characteristics of the WPT system are satisfied. Initially assuming $(\sqrt{L_P C_P})^{-1} = (\sqrt{L_S C_S})^{-1}$, an analysis of the control algorithm can be conducted. The first loop, namely the resonance tracking loop, is similar in structure to a digital phase-locked loop (DPLL). The purpose of the DPLL is to find and synthesize a switching frequency (f_{sw}) equal to $f_0 = f_{res}$, while the measurement of the phase informs whether the resonant frequency is achieved. For the topology under study, by measuring the voltage of the primary inductor on both ports and extracting the phase shift between them, it is indicated whether the drive and resonant frequencies are aligned. Fig. 27 shows the circuit as seen by the resonant control loop. V_p and V_{cp} represent the voltages at the inductor terminals (also the circuit's input voltage and the coupling plates' voltages, respectively). If the phase shift is greater than 90deg then $f_{sw} < f_{res}$, otherwise if it is lower than 90deg then $f_{sw} > f_{res}$. Only at $f_{sw} = f_{res}$ a 90deg phase shift is achieved (as shown at Fig. 26). This self-driving concept ensures in this LC configuration that the power conversion characteristics of the networks are optimized. For this type of high-Q - high voltage resonant converter, a DPLL is crucial, while a slight change is the drive frequency can drop the transferred power significantly. Variations in f_{res} may occur due to changes in C_m, or in the effective value of the passive components (as a function of voltage drop, temperature, degradation etc.). Since the theoretical analysis was based on the FHA (correct under resonant operating conditions), the DPLL has to be the fastest loop in the system in order to make it transparent to all the other control mechanisms. Assuming the resonant requirements are met, the primary circuit starts transmitting at f_{sw},, therefore developing a high voltage signal at the coupling plates.

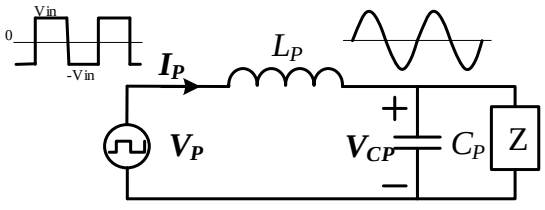

Fig. 27. The circuit as seen by the resonant loop

Whereas the primary side is at resonance, the secondary circuit receives a signal with a certain amplitude and frequency of f_{sw}. It is generally being assumed that the resonant tanks of both sided are tuned to one frequency. In practice, however, this is not the case due to non-ideal

components and parasitic effects. Any minor change in the reactive components' effective value, $f_{sw} = f_{res,\,prim} \neq f_{res,\,sec}$, departs the system from its optimal state. Fig. 28 shows the circuit as seen by the resonant control loop at the secondary side. Similar to the primary side, the secondary resonant tracking loop exhibits a 90deg phase shift between V_{cs}, V_s. In contrast to the primary side, which attains resonance by f_{sw} correction, the secondary circuit must alter its impedance matching network parameters (for the system presented by means of tunable inductor) in such a way that $f_{sw}=f_{res,\,sec}$. The co-existence of the two resonant tracking loops can be challenging, as changes at the secondary matching network affect the impedance Z (Fig. 27), setting the resonant frequency at $f_{res,prim} = \sqrt{L_P(C_P \,||\, Z)}^{-1}$, and therefore creating an non-converging correction loop. Two factors can prove useful for the foregoing problem: (1) the impedance Z (in the nearby resonance region) is mainly dictated by the capacitive coupling, so changes in L_s only slightly change Z; (2) The bandwidth of each loop is determined by the designer who in effect can "slow" a loop down by design, such that the system's variations become virtually negligible.

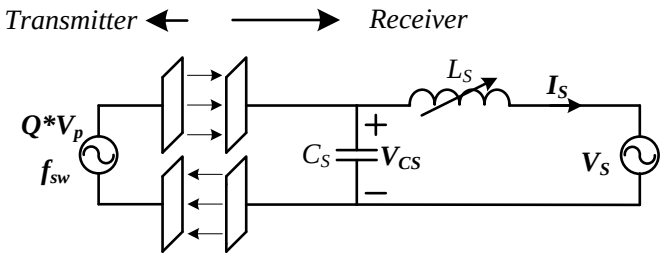

Fig. 28. Circuit as seen by the resonant loop at the secondary

Accordingly, the resonant tracking loop at the secondary is set to be slower than the primary side's resonant tracking loop, circumventing the stability problem and ensuring a fully tuned resonant network.

Once the system is tuned, the current loop comes into play (second loop of the primary). Current measurements at the primary (as shown in Fig. 17) are compared to a target current. If the current is too low - according to eq.(3.19) – the inductance is being decreased at the primary side, and vice versa. This loop only regulates inductance at the primary as no access to the secondary is available (later work should include wireless communication). Considering that the change of inductance imposes a new resonant frequency, the foregoing changes must occur before the primary resonant loop locks into the f_{res}, and moreover, before the secondary side locks into the same f_{res}. In other words, the current loop is by necessity the slowest of all three control loops. Fig. 29 shows the overall flow chart of the controller tuning procedure. Block diagrams and loop analysis are given in the next section, and their practical implementation is discussed in chapter 4.

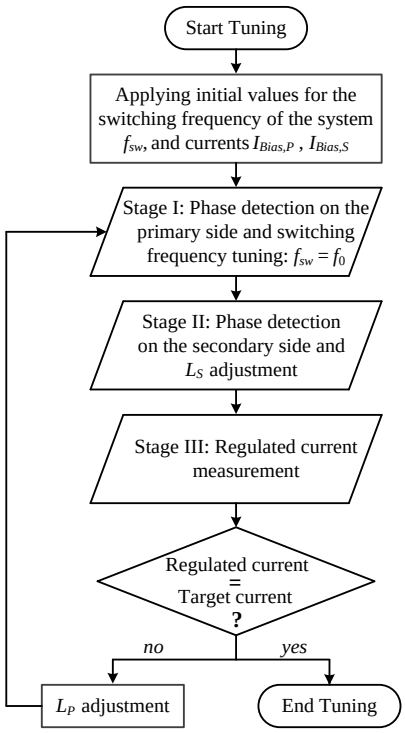

Fig. 29. Flow chart of the controller's tuning procedure

3.3 Controller Architecture:

As a follow up to the description of the control algorithm given in the previous section, a simplified functional block diagrams that describes the dynamic behavior of this self-tuned system, is depicted in Fig. 30. The diagram comprises linear and non-linear transfer functions to reflect the specific operation of each 'transformation unit'. The diagram of the control scheme at the primary circuit includes two major loops to emulate a current source to the transfer plates as shown in Fig. 30(a). A third independent loop is located at the secondary side to correspond the receiving network to the signal frequency as shown in Fig. 30(b). To optimize the the primary and secondary circuits, the bias driver of the variable inductors can be designed as a closed feedback loop configuration in order to maintain a forced current control. This step should reduce the order of the outer feedback loop, and would therefore make it easier for the overall system to stabilize. The suggested alternative is addressed in section 4.4.2 of this paper. By employing self-calibrating frequency loop and adjusting the system parameters, the regulation of the primary's output current, I_{out}, can be obtained concurrently with the system being in a resonant state (while soft-switching conditions are met).

Starting from the left side of Fig. 30(a), I_{target} denotes the target regulated current from the primary to the secondary, and I_{out} is the present current supplied to the secondary. $I_{sns,out}$ denotes the output current. I_e is the error between the target and supplied currents. It feeds the *Compensator* G_{comp1} unit, that adjusts the reference signal to the Bias-Buck. $D_{Buck,P}$ denotes the control signal for the bias current driver. The bias driver in this study is realized by a buck

converter and its transfer function is labeled B_P in the block diagram. The bias current for the inductor L_P can be expressed as

$$I_{Bias,P} = D_{Buck,P} B_P(s) = \frac{D_{Buck,P} V_{Buck}}{sL_{Bias} + R_{DCR}} \tag{3.22}$$

where L_{Bias} is the inductor of the buck converter, R_{DCR} is the dc resistance of the inductor, D_P and V_{Buck} are the duty-cycle and the input voltage of the buck converter, respectively.

H_{LP} represents the bias winding such that the relationship between the bias current and the primary side inductance is

$$L_P = H_{LP}(I_{Bias,P}) \tag{3.23}$$

Lastly, K_f is the response of the matching network - combined with power-stage - to the variable inductor generated by H_{LP} (the ratio of the regulated current I_{reg} to a change of the resonant characteristics).

The bottom block diagram in Fig. 30(a) details the transfer characteristics of K_f. The output of H_{LP} determines the resonant frequency f_0 of the CPT system such that

$$K_{res,P}(L_P) = f_0 = \frac{1}{2\pi \sqrt{\underbrace{H_{LP}(I_{Bias,P})}_{L_P} C_P}} \tag{3.24}$$

Assuming that the frequency tuning constitutes the fastest control loop in the system, f_0 is constantly compared to the switching frequency f_{sw} of the full-bridge to guarantee that $f_{sw}=f_0$. K_Φ denotes the gain of the phase detector. Consequently, the phase detector can be envisioned as a module that translates frequencies into phases and then compares between them. The outcome of the phase detector, $V_{PD,P}$ represents a proportional phase mismatch between the inputs of the phase detector for every switching cycle of the system. $V_{PD,P}$ is filtered by a digital-low-pass filter (DLPF). The voltage V_f is then translated by the DCO unit to a drive frequency for the combined power-stage and LC tank setup, which in turn generates the desired target current.

If the outer compensator is designed to be with relatively slow dynamics (yet with reasonable phase margin and loop gain bandwidth) compared to the inner control loops, then the dynamics of the bias converter (DCO) and power-stage (including the LC tank) units are transparent to the outer regulated current loop. This implies that L_P – when adjusted sufficiently slow - ensures resonant conditions and renders K_f constant.

Fig. 30 (b) depicts the functional block diagram of the secondary's control loops. The operating resonant frequency of the system is compared throughout a phase detector to the resonant frequency of the secondary. It should be noted that for stable operating CPT system, we have

$f_{0,S}=f_{sw}=f_0$. In line with above relationships in the primary side, the output signal of the secondary's phase detector $V_{PD,S}$ is filtered and compensated by Compensator G_{comp2} (which also includes a DLPF) producing $D_{Buck,S}$, a modulation signal for the secondary convert's driver, proportional to the phase mismatch between the drive frequency, and the current resonant frequency of the matching network at the secondary(do yourself a favor and break this phrase into 2-3 parts, then revised them. I was already lost towards the middle of this excruciating sentence). Similar to the analysis of the bias current at the primary, a buck converter generates the $I_{Bias,S}$ current for the variable inductor L_S. The resultant inductance value of L_S generates a new resonant frequency $f_{0,S}$ until the phase difference $\varphi_{diff,S}$ equals 90°. In the latter case, the transmitting and receiving sides are matched and the system is operating under optimal power transfer conditions.

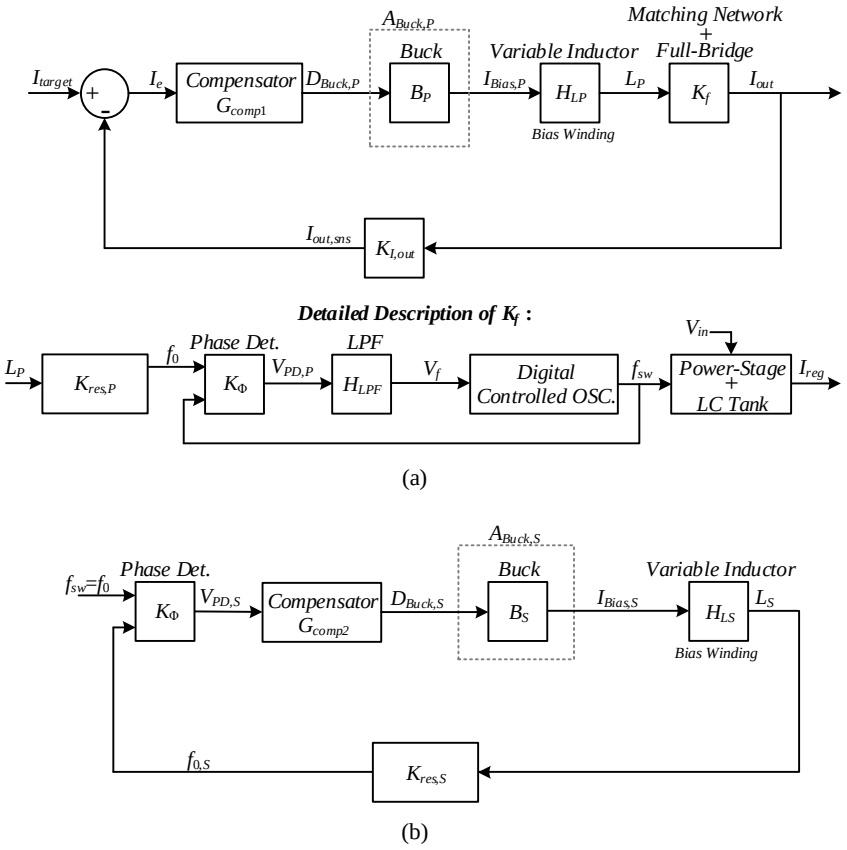

Fig. 30. Simplified functional block diagram of the multi-feedback controller: (a) Primary side control loops, (b) Secondary side control loops

4 Practical implementation:

The following chapter covers the practical implementation of the control blocks as discussed in the previous chapter. The control elements are presented in conjunction with the control loops hierarchy.

4.1 Phase Detector:

4.1.1 XOR Phase Detector:

The Phase Detection for both transmitting and the receiving sides in this study has been realized as illustrated in Fig. 31. Applying this method requires the conversion of analog signals into logical binary representation. In the square waveform case this conversion is trivial, as the binary representation of the positive and negative ends of a sinusoidal waveform are logical *'0'* and *'1'*, respectively. In double sided LC topology the voltages at the inductor's terminals are normally higher than the operating logic voltage V_{DD} (V_{DD}=5V in our case), and have a superimposed AC component higher than the DC component (at V_{CP}: V_{DC}=0 for full bridge inverter, V_{DC}=V_{in}/2 for half bridge inverter), therefore generating negatives voltages. Since electronic components have a limited range of input voltages/currents (outside which they are likely not to function properly) the measured signals must be "corrected". Therefore, a simple high resistance voltage divider network is used to downscale the voltages V_P and V_{CP} (V_S and V_{CS}) into 0-V_{DD}/2 [V] region, therefore overcoming the amplitude-related problem. The resistor networks should be planned with care, as voltages may vary (especially for different C_m values). A DC offset component with an amplitude of V_{DD}/2 is then added to the high-frequency scaled signals, ensuring that the component's input restrictions are not violated. Moreover, the DC offset avoids the zero-crossing problem in single supply comparators.

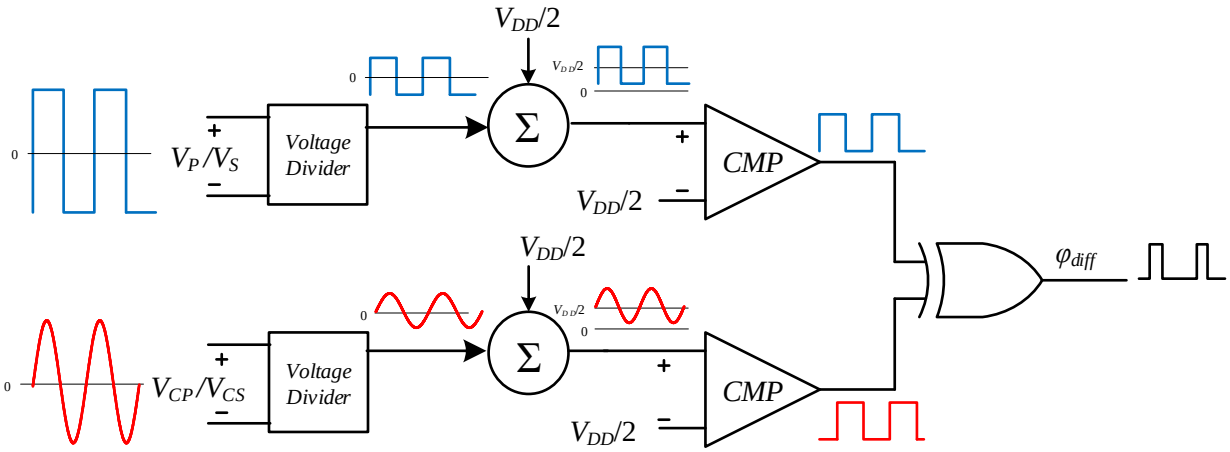

Fig. 31. XOR Phase Detector

The processed signals are then compared with $V_{DD}/2$. The output of each comparator is a square waveform of the analog voltage waveform. Next, the outputs of the comparators enter a XOR logic gate. As mentioned in Section 3, the phase difference between the signals is 90° under resonant operation as shown in Fig. 32(a). Consequently, the output of the XOR, φ_{diff}, is a square wave with 50% duty-ratio and a doubled frequency. For a case that resonant operation is not satisfied as shown in Fig. 32(b), the duty-ratio of φ_{diff} is either above or below 50%.

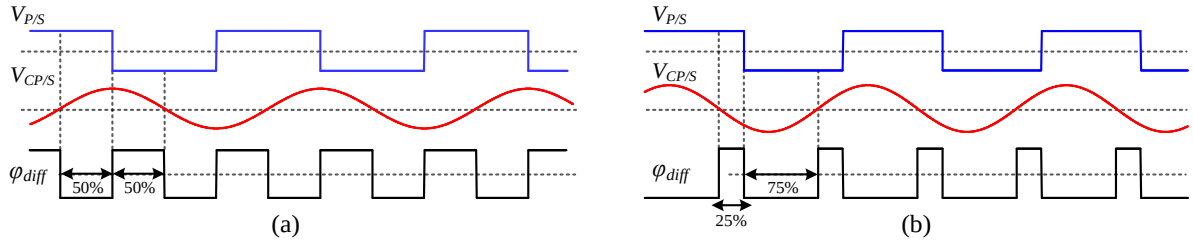

Fig. 32. Signals of the phase detector: (a) Tuned CPT system operating in resonance; (b) Non-tuned CPT system

Reaching the φ_{diff} duty-cycle can be carried out with a simple RC low pass filter, but this would require additional ADC. Therefore, a digital low pass filter is implemented instead.

4.1.2 Digital LPF:

As the output of the XOR gate is a PWM signal with twice the frequency of the drive signal (and unknown duty-cycle) and furthermore since both may vary, the Digital Low Pass Filter essentially operates as an adaptive '0'and '1' ratio detector. Although it has the highest bandwidth, a trivial count of the number of rising clocks at '0' and at '1' values of the φ_{diff} signal over a single XOR period may not suffice, due to limited clock frequency and non-synchronized signal nature. Performing the same procedure over N XOR rising edges, as shown in Fig. 33 (b), increases the resolution of the measured duty-cycle accuracy, at the expense of limiting the bandwidth by 1/N factor. Linking the averaging process to N rising edges of the XOR gate rather than to a constant number of clock's rising edge enables to maintain the same control dynamics at any driving frequency. Therefore, it provides an adaptive low-pass filter. Once summed over N cycles, the number of '0's and '1's determines the phase as follows:

$$Phase = \frac{'1'}{'0'+'1'} * 180º \qquad (4.1)$$

In order to achieve a 90deg phase shift, the number of '0's and '1's must equal, but this only confines eq.(4.1) to a singular case. If N is high enough (above 20), a resonance can be settled by creating two phase shift thresholds, namely by setting '0'-delta1<'1'<'0'+delta2 as a 90deg phase shift. Eventually, the '1's to '0's ratio is the integer representation of the phase that is delivered to the compensator.

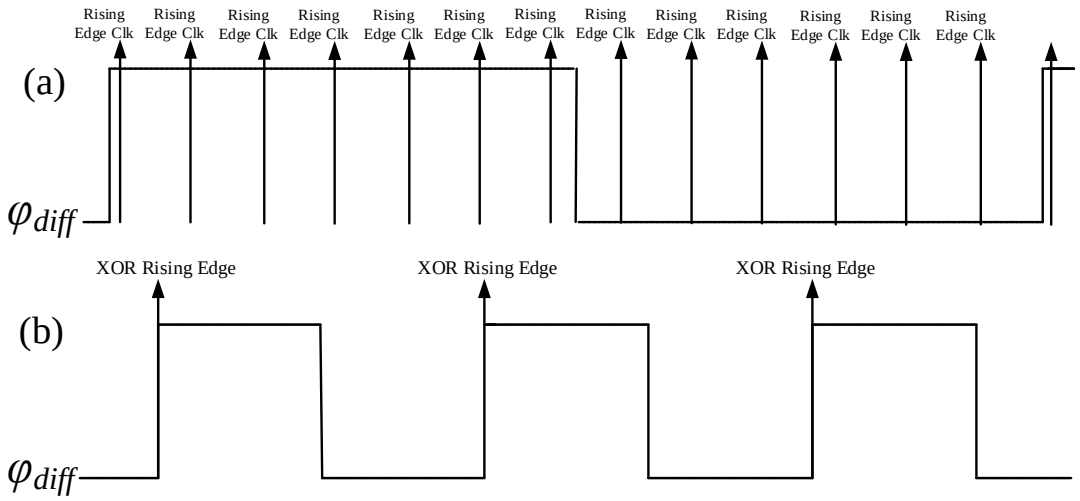

Fig. 33. (a) Single cycle duty-cycle detection; (b) N cycles duty-cycle detection

4.2 Limit-Cycle Oscillations in Digitally Controlled Resonant Converters

4.2.1 DCO- Digitally Controlled Oscillator

A major issue that should be considered when designing closed-loop resonant based WPT systems are limit-cycle oscillations, which result from the presence of the quantizing units of the controller, i.e., analog-to-digital converter (ADC) and the DCO (assuming the compensators do not add quantization error)[47]. The prime cause for limit-cycle oscillations in resonant converters are the input-output gain variations as function of the frequency. In capacitive WPT systems that operate at resonance, the effective impedance is very high because of the coupling plates. In this case, a very high parallel quality factor Q is considered, which is translated to a very high voltage gain. In addition, as discussed in the previous sections, one of the key parameters to successfully regulate the power is to tune the system to the resonant frequency. However, to guarantee optimal power transfer conditions soft-switched operation should be satisfied, meaning that one needs to generate a drive frequency which slightly above the resonant frequency. To this end, a very sensitive calibration is required, one which may also result in limit-cycle oscillations; the reason being that in resonant converters the frequency resolution highly depends on operating conditions and the location of the drive frequency with respect to the network's resonance [48]. Moreover, another issue pertains to the quality factor Q; since it is not constant but rather depends on the capacitive medium characteristics (distance, alignment, etc.), it affects the input-output gain of the system. In light of all this, to ensure proper operation, the worst-case for the resolution sensitivity should initially be taken into account. This (i.e., the worst-case) coincides with the highest Q that the system can have. Thus, the ADC and DCO units in this study have been designed such that limit-cycle oscillations are being compensated by design. The main criterion for determining the existence of limit-cycle oscillations in resonant systems relies on the comparison between the LSB value (i.e., resolution) of the ADC and the output signal variation due to an LSB change of the control[48],

[49]. In other words, a necessary condition for no limit cycles is having the variation of the output ΔS_{out}, due to an LSB change of control, below the ADC resolution Δ_{ADC} [49]

$$\Delta S_{out} < \Delta_{\mathrm{ADC}} = \frac{V_{\mathrm{ADC}}}{2^{N_{\mathrm{ADC}}}} \tag{4.2}$$

where V_{ADC} and N_{ADC} are the ADC reference voltage and number of bits, respectively.

Digitally synthesized frequency is normally carried out by timers that are programmed to reset at a desired value while maintaining a fixed 50% duty ratio[50]. The generated frequency can be expressed as follows

$$f_{\mathrm{DCO}} = \frac{1}{N_{per} TB} \tag{4.3}$$

where N_{per} is an integer and TB is the time base of the unit clock. The frequency resolution can be calculated as the LSB change in N_{per}

$$\Delta f_{\mathrm{DCO}} = \frac{1}{N_{per} TB} - \frac{1}{\left(N_{per} - 1\right) TB} \approx \frac{1}{N_{per}^2 TB} = TB f_{\mathrm{DCO}}^2 \tag{4.4}$$

From eq. (4.4), it can be well observed that the frequency steps of the DCO are limited by the system's clock frequency, and are proportional to the square of the operating frequency. At lower running frequencies, the frequency resolution would outdo the resolution at higher frequencies. Consider, for example, a 50-MHz FPGA clock that generates drive signal at approximately $f_{DCO}=1MHz$, namely $N_{per}=25$. Assuming that a slightly higher drive frequency is required, changing N_{per} to 24 sets f_{DCO} at $1.04166\ MHz$, that is, a 41 kHz increment. Such coarse DCO tuning cannot satisfy an adaptive high-Q WPT system. By contrast, if a higher resolution than the one obtained by the system DCO is required, an effective fast dynamics and low distortion frequency dithering procedure should be adopted, as will be discussed shortly.

4.2.2 Enhancing Frequency Resolution by Dithering:

Frac-N dither is facilitated by toggling the DCO's time period between (N_{per}) and ($N_{per}\pm1$) at a defined rate that is varied by the target frequency. The "dither factor" 'n' is the number of DCO cycles needed to achieve the fractional frequency. Dithering is achieved by (n-1) DCO cycles with N_{per} period, plus a single cycle with period of $N_{per}+1$ or $N_{per}-1$. Detailed theoretical analysis, constrains and limitations of the frequency modulation method presented here, are discussed in [50]. In this work, the enhancement of frequency resolution through Dithering can be regarded as 'frequency averaging'. Now, consider a high-Q resonant WPT converter operating in the near resonant region and driven at a given f_{sw} frequency. Once f_{sw} changes, it would take Q cycles of the DCO before the circuit settles into its new steady state operating conditions. Assuming $n<Q/8$, the effective drive frequency is:

$$f_{DCO\_dit} = \frac{1}{[(n-1)N_{per}+(N_{per}+1)]/nTB_{clk}} = \frac{1}{(N_{per}+\frac{1}{n})TB_{clk}} \quad n = 1,2,3 \ldots \tag{4.5}$$

and the frequency resolution is

$$f_{res\_dit} = \frac{1}{(N_{per}+\frac{1}{n+1})TB_{clk}} - \frac{1}{\left(N_{per}+\frac{1}{n}\right)TB_{clk}} \approx \frac{1}{n(n+1)N_{per}^2TB_{clk}} = \frac{TB_{clk}f_{DCO}^2}{n(n+1)} \tag{4.6}$$

From eq. (4.6) it is easy to see that the dithering improves the resolution by a factor of n^2. Fig. 34 shows the dithering process flow chart. If, for instance, the new target frequency corresponds to $N_{per}=30.25$, then the driving sequence of 30,30,30,31; 30,30,30,31; .. brings us (in average) to the desired period.

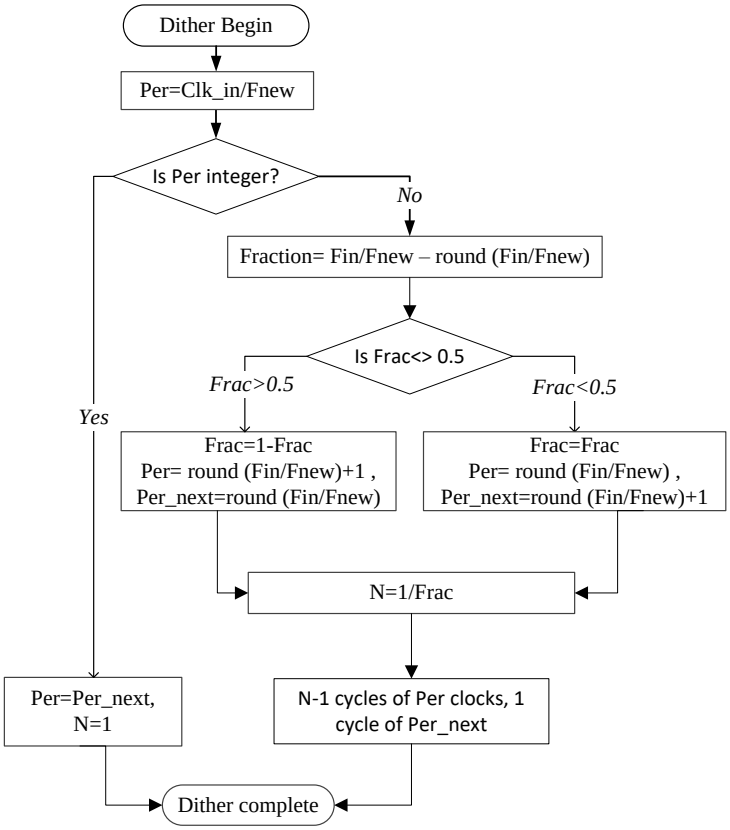

Fig. 34. Dithering process flow chart

Fig. 35 shows the input/ output behavior of the dither block. F_{clk} represents the controller's clock frequency. F_{target} is the target drive frequency as being set by the compensator with respect to the phase shift error. Also, the following denotations apply to the output: (1) n- "dither factor"; (2) PER- number of clocks before flipping drive signal polarity, for (n-1) times; (3) PER_NEXT- last cycle's length (PER±1); hence, the high-resolution DCO is accomplished using a simple counter.

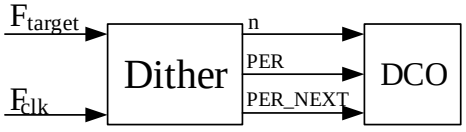

Fig. 35. Dither Block Inputs/ Outputs

4.3 Current Sensing Circuitry:

The multi mixed-signal controller requires various measurements of the operating conditions in the WPT system. A key measurement of the system is the regulated current, I_{reg}, to the capacitive medium. However, this high-frequency current is not trivial to measure, and sensing techniques for measuring, such as current transformers, may result in complex sensing circuitry. The current-sensing employed in this study is based on a two-step conversions: (1) Current to Time; (2) Time to Integer.

4.3.1 Current to Pulse Length Conversion:

Because the controller in this work is digital, an ADC is necessary to process the current readings. The sinusoidal nature of the current and the varying drive frequency make the momentary value of the current meaningless, whereas the peak current value becomes a key parameter. The peak detection is based on an active half-wave rectifier configuration, as shown in Fig. 36.

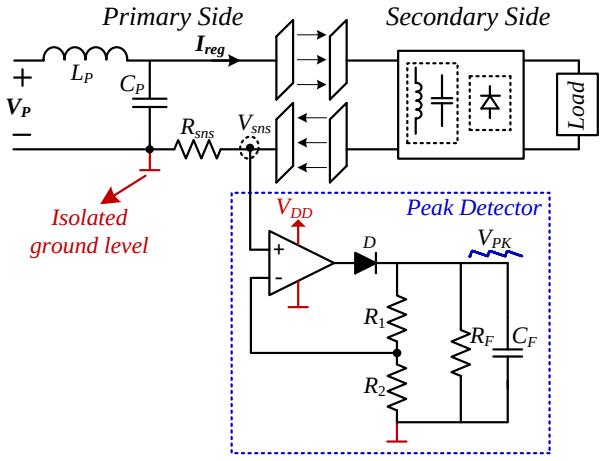

Fig. 36. Circuit diagram of the current-sensing setup

The sensed current is converted to a proportional voltage signal, V_{sns}, by flowing through the resistor R_{sns}[47], [51]. Moreover, as R_{sns} is in the [mΩ] range and in series connection to the coupling interface's impedance, it plays no role in the analysis or in the power flow. The peak detector is implemented around an operational amplifier to compensate for the voltage drop on the rectifying diode *D*. To reduce the losses related to the diode, a Schottky diode is being used. This diode has a relatively low forward voltage and zero reverse recovery time, which further improve the sensor performance. The time constant of the peak detector is set to be approximately ten times the period of the sensed sinusoidal signal. The latter ratio helps to filter out the ripple and smoothly follow the peak value of the signal. It should be noted that a key feature of the sensors of the implemented CPT system (and in particular of the current sensing

circuitry) is to provide an isolated ground reference level to the sense resistor, as well as for the peak detector circuit (Fig. 36). By doing so, the limitations due to sensing relative to a floating voltage node are removed. This configuration also improves the signal to noise ratio. Once the proportional to peak current voltage is extracted (V_{PK}), it is fed into the One-Shot circuit as shown in Fig. 37. The output pulse length is given by:

$$T_{pulse} = RC \ln\left(\frac{V_{dd}}{V_{pk} - V_{th}}\right) \quad (4.7)$$

Where V_{th} is the V_{IL} of the NOR2 logical gate. The triggering signal is sent from the controller in keeping with the sampling requirements. The output signal has a digital configuration that permits subsequent digital processing.

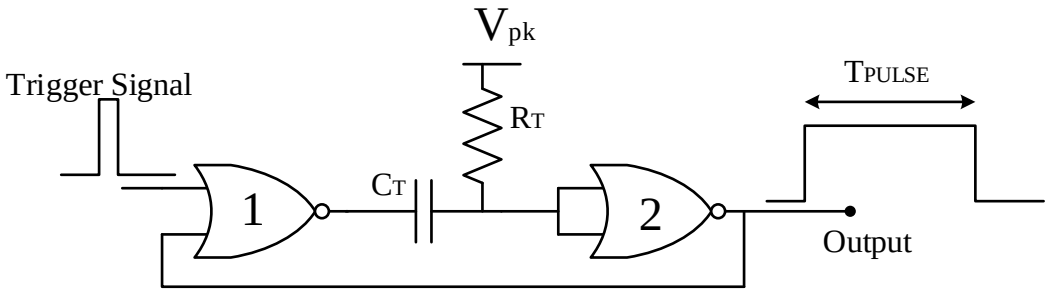

Fig. 37. NOR One-Shot circuit

4.3.2 Pulse Length to Integer Conversion:

When the pulse reaches the controller, the pulse length indicator converts time to integer. As a single pulse length is within a range of hundreds of ns, a simple 200MHz clocked counter gives accurate results. It should be noted that although the current sampling rate can be very high, it is nonetheless advised to average the current sensing results over several samples, since the current measurement serves the current control loop which has significantly lower band-width.

4.4 Variable Inductor:

4.4.1 Variable Inductor:

One possible implementation of variable inductor is shown in Fig. 38(a), with a magnetic structure able to change the inductance of the inductor, irrespective of other power transfer circuit parameters [52]. The structure comprises an E-core type magnetic element wherein the primary inductor is constructed in the mid-gapped leg. The bias/control winding is formed on the outer, non-gapped part, and their windings are connected in series but with opposite polarity. By doing so, the AC coupling between the center leg to the bias winding is cancelled. Passing DC current through the auxiliary winding would partially saturate this portion of the core, resulting in variable inductance, as illustrated by Fig. 38 (b).

The inductance value L can be found with the aid several design parameters such as: the number of turns n, air-gap l_g, and effective magnetic path length l_e. Hence, L can be expressed as [53]

$$L = \frac{n^2 \mu_0 A_e}{l_e} \frac{\mu_r(I_{Bias})}{1 + 2\frac{l_g}{l_e}\mu_r(I_{Bias})} \tag{4.8}$$

with μ_0 being the air permeability, μr the magnetic core permeability, and A_e the core area. μ_r depends on the bias current, I_{Bias} ,and can be obtained from the manufacturer data or experimentally [52], [53]. A simplified expression of μr is given by

$$\mu_r(I_{Bias}) = \frac{\mu_{mi}}{1 + \left(H(I_{Bias}) / H_{\text{pole}}\right)^j} \tag{4.9}$$

where μ_{mi} is the permeability initial value, i.e., $\mu_{mi} = \mu_r$ (H = 0), H_{pole} is the magnitude of the saturation field and j sets the permeability slope. The variable H is proportional to the bias current, and is expressed as follows

$$H(I_{Bias}) = nI_{Bias} / l_e \tag{4.10}$$

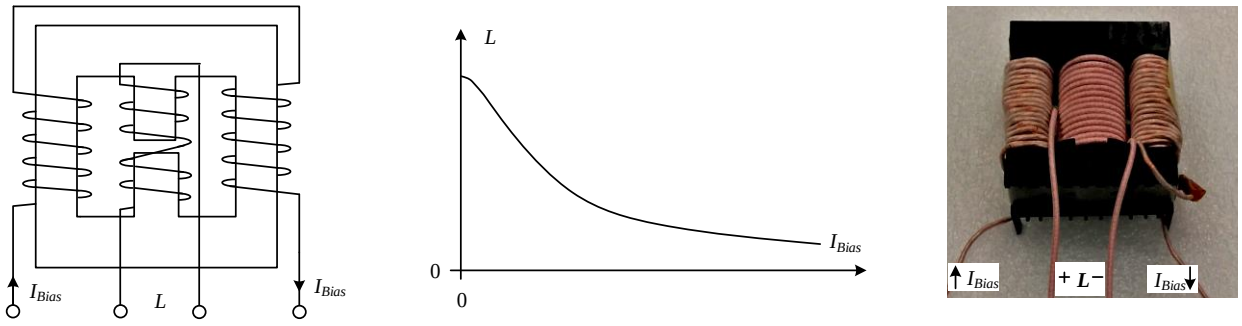

(a) (b) (c)

Fig. 38. (a) Variable inductor practical implementation; (b) Relationship between the inductance value and the bias current; (c) Practical Implementation

Fig. 38(c) shows the practical implementation of the variable inductor.

4.4.2 Constant On-Time Buck:

As a follow up to section 3.3 of this paper, an alternative for bias current control is presented in this section. We should note that this proposal was experimentally tested and verified, yet eventually, the overall tuning process was accomplished utilizing the direct Buck control as shown in Fig. 30. This approach is presented as an optimization option. According to [52], the changes in the inductance are non-linear with regard to the bias current, as shown in Fig. 38 (b). Maintaining a constant dc current is essential for constant effective inductance. Therefore, a closed loop dc current source was implemented based on a Constant-On Time Buck Converter. Fig. 39 (a) shows the control block diagram, with respect to the signals at Fig. 30. Fig. 39(b) shows

the schematic structure of the circuit as implemented on the board - a Half-Bridge module with series connected inductor and resistor. It is similar to a synchronous Buck- Converter, excluding the output capacitor and load. The control mechanism starts with sensing the I_{bias} current using R_{sense} resistor. The proportional current representation, $I_{bias,sns}$,is then compared with I_{ref}, which is the resultant of a low-pass filtered $D_{Buck,P}$ signal received from the controller. Whenever I_{ref} is higher than I_{bias}, the comparator triggers the One-Shot module (of similar structure to the module in section 4.3.1).

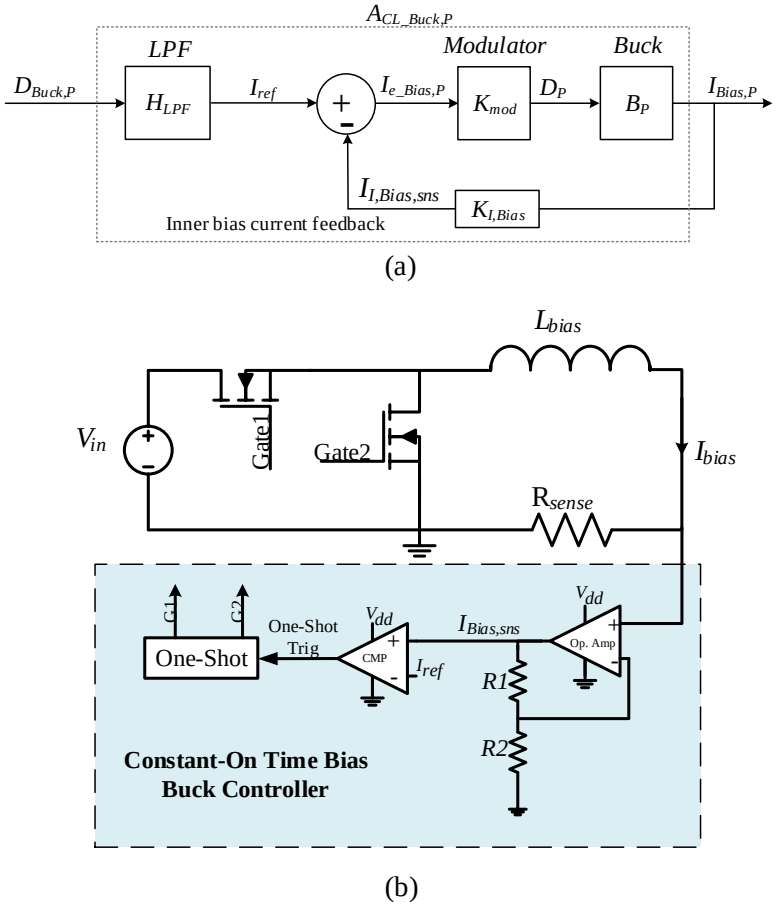

Fig. 39. Constant On-Time Bias Buck: (a) Control Blocks Diagram; (b) Schematic Implementation;

Triggering the One-Shot creates a drive signal that activates Gate1 for a constant period of time according to $T_{on}=0.35RC$, and according to the capacitor and resistor set in the One-Shot module. Fig. 40 shows typical waveforms of the bias buck controller, with respect to the circuit in Fig. 39. Considering low V_{in} (2-5 V) and T_{on} in the 0.1-2us range, the bias current ripple can go below 1mA, setting constant I_{bias} current and therefore a constant inductance.

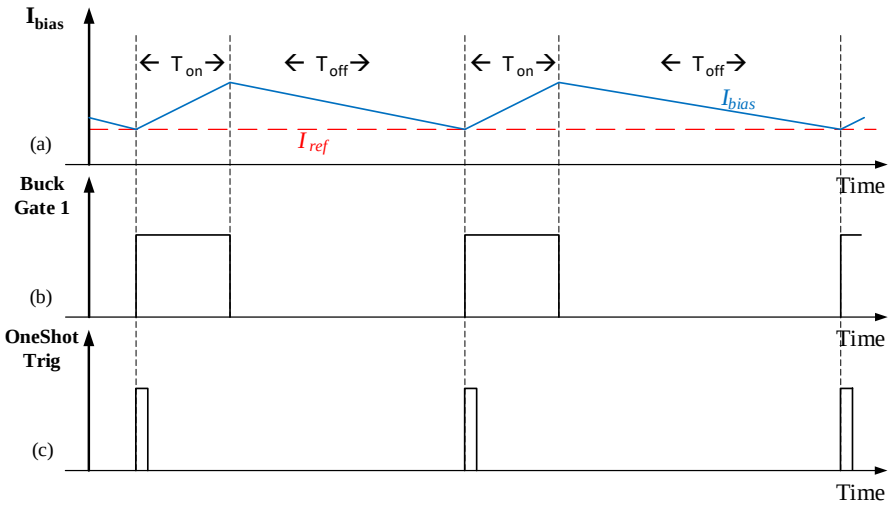

Fig. 40. Constant On-Time Bias Buck typical waveforms

4.5 Protection Circuitry:

4.5.1 Over Voltage Protection:

As discussed in the previous chapters, the circuit has high-frequency, high-voltage properties. Thus, it is potentially dangerous to the circuit and the surrounding. Assuming proper operating conditions, an over-voltage may occur only at the coupling plates at the transmitter's and/or at the receiver's coupling plates. Over-voltage faults can be categorized into four groups (with respect to the design given): (1) $V_{Cp/s} * R1/(R1+R2) > Vdd/2$, in which case the sensing circuitry reliability is limited; (2) The airgap spark stands at [30KV*cm]. Exceeding this limit results in an electrical arcing; (3) According to [54], high-frequency operation has amplitude limitation in order not to make the electric field radiative; (4) Components' voltage rating. Therefore, the over-voltage sensing was implemented using op-amp as a buffer, followed by a comparator, as shown in Fig. 41. The output of the comparator enables the gating block, and once V_{cp} exceeds V_{ref}, the controller turns off the system.

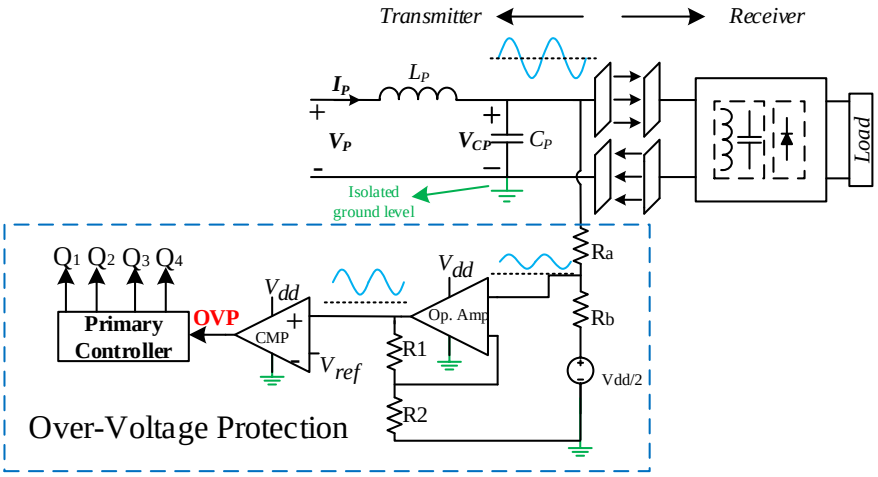

Fig. 41. Over-Voltage Protection Circuit

4.5.2 Over-Current Protection:

Similar to the over-voltage protection, the Over-Current protection goal is to avoid system failure risks in the WPT system or health hazards to the user. The purpose of applying additional "protection loop" (besides protecting the user and the system), is to monitor the system's behavior and functionality not just at the coupling plates, but throughout the overall flow. The current under discussion is I_p, as it facilitates all of the currents at the primary side. The system may encounter a state of over-current when the following conditions are fulfilled: (1) $C_m \rightarrow 0$, creating unloaded series LC resonant tank; (2) The LC tank is shorted, and the circuit ceases to function; (3) The current exceeds the components current rating. The sensing topology is similar to the current sensing shown earlier, with a comparator at the output of the peak detector block, as shown in Fig. 42. The output of the comparator is another enabler to the gating block, such

that both the voltage and the currents should lie within a valid range for the system to operate. Alternatively, the current sensing may utilize the $R_{ds,on}$ resistance of the transistors in the power stage, increasing the Q factor and minimizing loses.

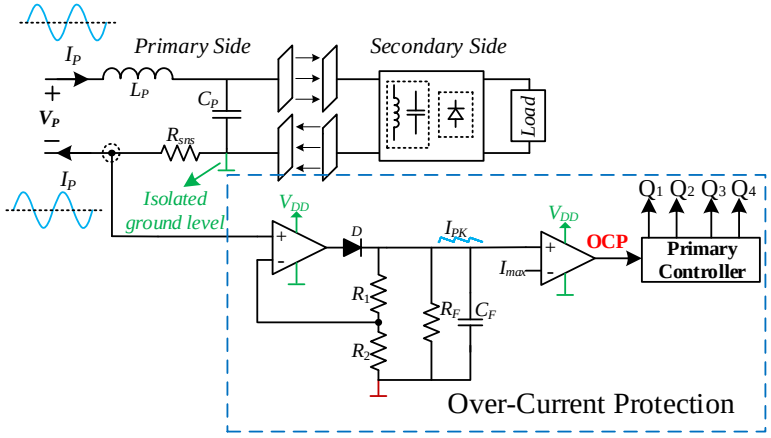

Fig. 42. Over-Current Protection

5 Experimental Verification:

To validate the operation of the adaptive multi-loop controller, an experimental double-sided LC CPT system prototype has been assembled, as shown in Fig. 43.

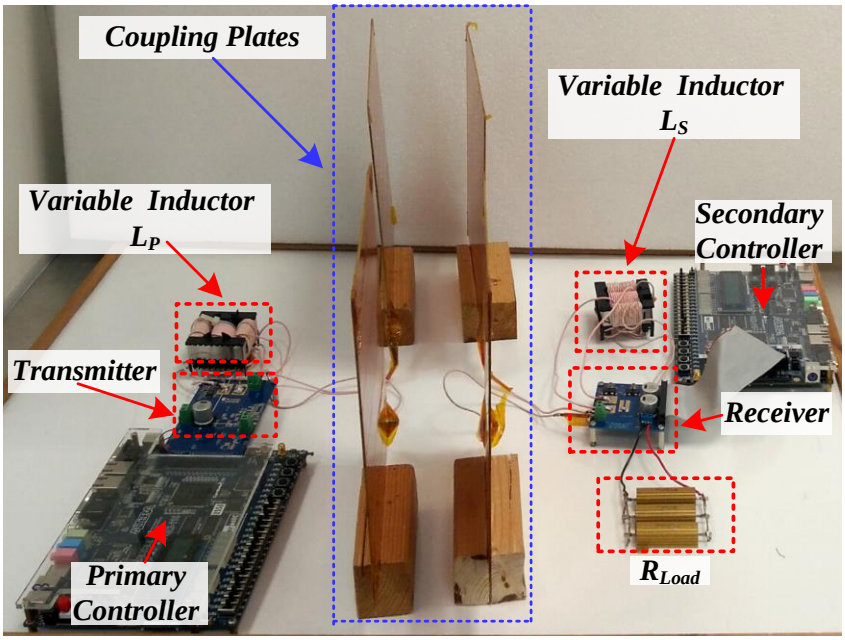

Fig. 43. Experimental setup of double-sided LC CPT system

The coupling interface is attained by placing the four 30x30cm copper plates in two pairs facing each other, (Fig. 43). This in turn forms a pair of coupling capacitors with a dominant series capacitance (relative to the cross capacitance, and self-capacitance).

5.1 Variable Inductor:

The custom-designed variable inductor was realized using two E-core type ETD49-3F3 magnetic elements. Both L_p, L_s are assembled using the same number of turns, types of wire and lengths for maximal symmetry. Using external current source, inductance measurements as a function of I_{bias} were taken for L_p, L_s and the expected resonant frequency was calculated considering parallel capacitance of ~250pF, as shown in Fig. 44.

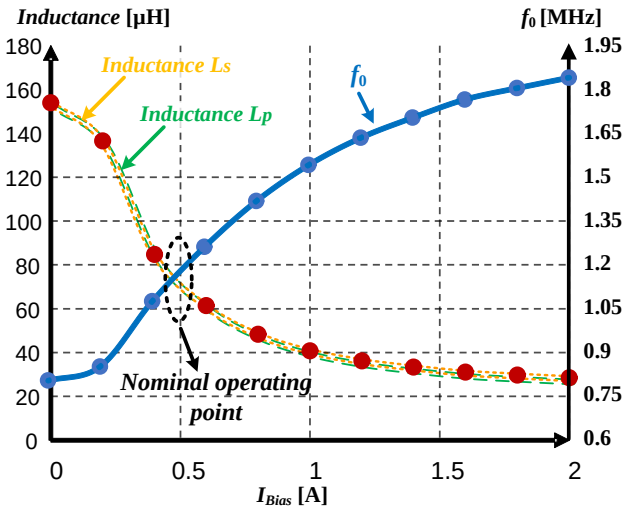

Fig. 44. L_p, L_s vs I_{bias}, and the expected resonant frequency

Continuous inductance regulation demands a controlled DC current source. Hence, the L_{bias} inductance is usually within the range of a few mH. Utilizing L_{bias} as the inductor of an unloaded Buck DC-DC converter lowers the total component count as well as the size and complexity of the system. The unloaded buck configuration and two control mechanisms options for maintaining constant current are implemented at the board, as shown in Fig. 45.

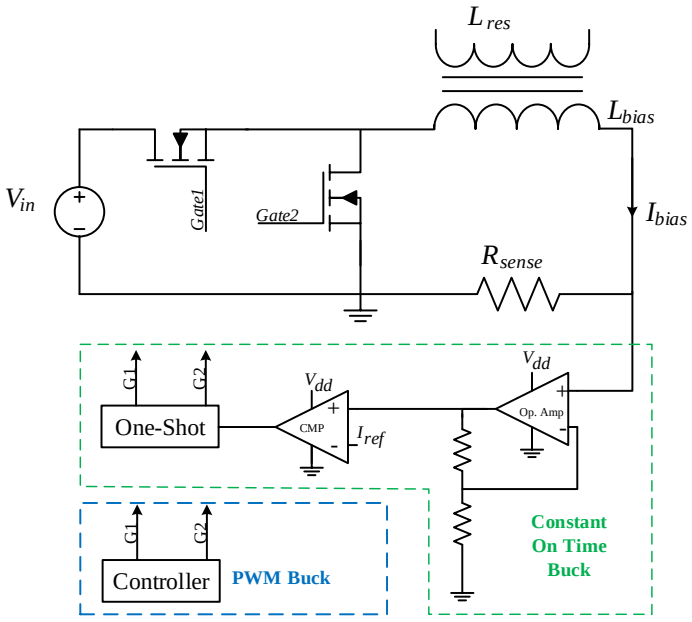

Fig. 45. Lbias Control Current Source

The Constant On-Time Controller is the preferable option for experimental setup, as it simplifies the control dynamics of the systems. In final products, variations in the drive frequency can affect other sub-circuits. In order to verify an alternative control method, a fixed frequency PWM drive signal - generated by the controller - was applied to Buck's gates directly, and by doing so it cancelled the I_{bias} control loop. While the two methods produce the same

constant current (as shown in Fig. 46) it is important to realize the choosing either of them affects the overall system control algorithm and limitations.

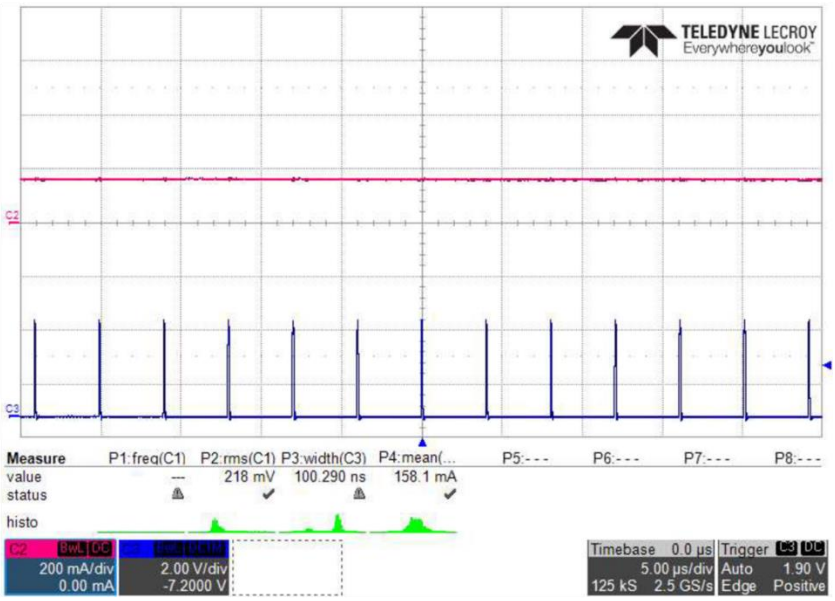

Fig. 46. Red- I_{bias} current; Blue- Drive signal

For both methods, high drive frequency (1MHz or higher) and low input voltage (1-5 V) assist in minimizing the current ripple, therefore stabilizing the effective inductance.

Table 1: Ibias Experimental Prototype Parameters at Nominal Operation

Parameter	Value/ Type
V_{in}	1-5 [V]
I_{out}	0-2.5 [A]
L_{bias}	~6 [mH]
Gate Transistors	SI2318CD
Driver	LM27222
Op. Amp	TLV3541
Comparator	TLV3501
NOR Logic Gate (One-Shot)	NL27WZ02

5.2 Resonant loop:

As discussed in previous the sections, the resonant tracking loop initially converts the voltage waveforms at the inductor nodes to square waveforms, which then feed the inputs of a XOR logic gate.

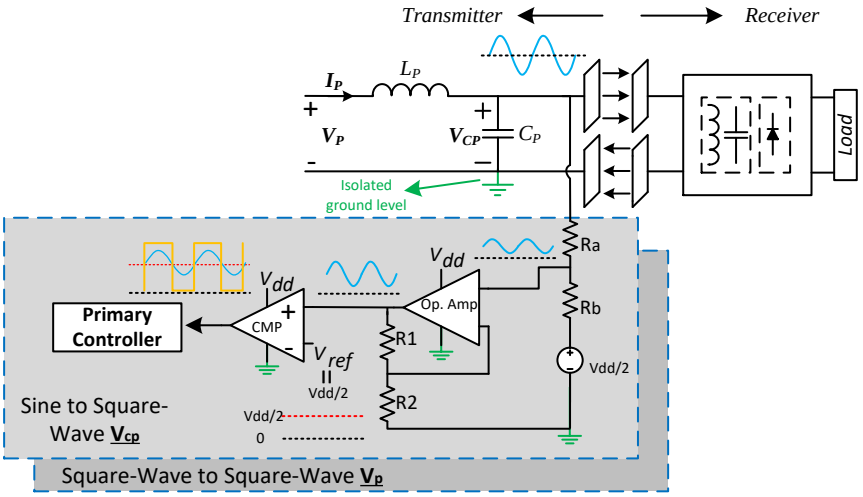

Fig. 47. Sine to Square-Wave converter

Fig. 47 shows the waveform converter sub-circuit. Both voltage signals sensors are configured exactly the same, apart from the R_a, R_b resistors. Fig. 48 shows the V_{cp} sinusoidal voltage wave, and the corresponding square wave.

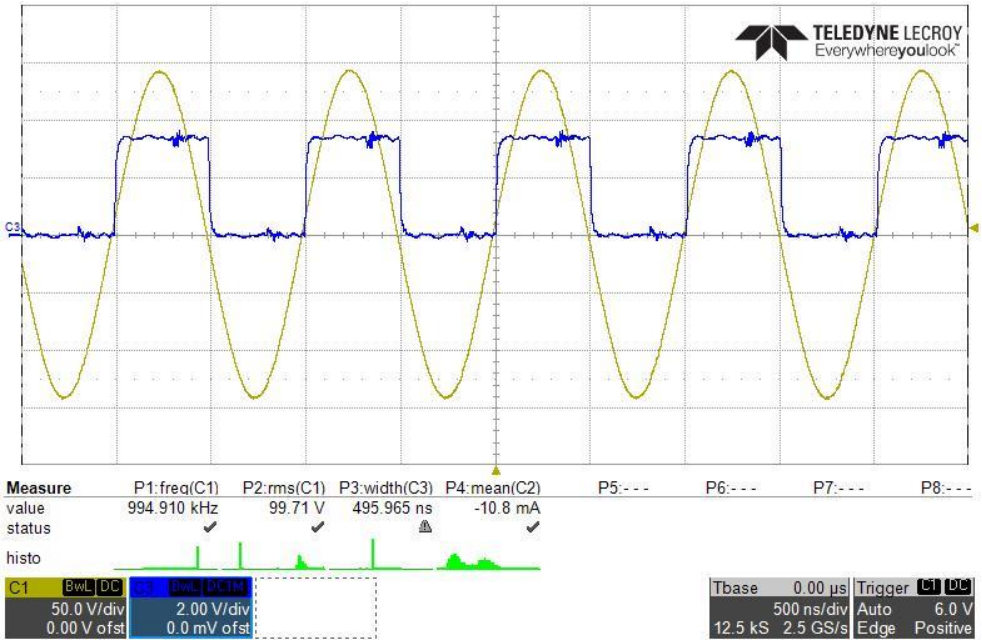

Fig. 48. Yellow- Vcp; Blue- Converted waveform

While V_{cp} voltage wave must be sensed, the V_p voltage wave is (almost) identical to the drive signal generated by the controller, excluding a constant time delay of 50ns due to buffers and isolators. As this delay is constant, the sensing circuitry can be reduced to a single voltage sensor, while the controller internally delays the output drive signal by 50 ns and addresses it as a square wave voltage input. The V_p, I_p waveforms whilst the resonant tracking loop is searching for the resonant frequency shown in Fig. 49. Though this may seem like a slow process, it

confirms that the resonant loop identifies the target frequency (1.04MHz) even when its initial drive frequency value is far from resonance (520kHz).

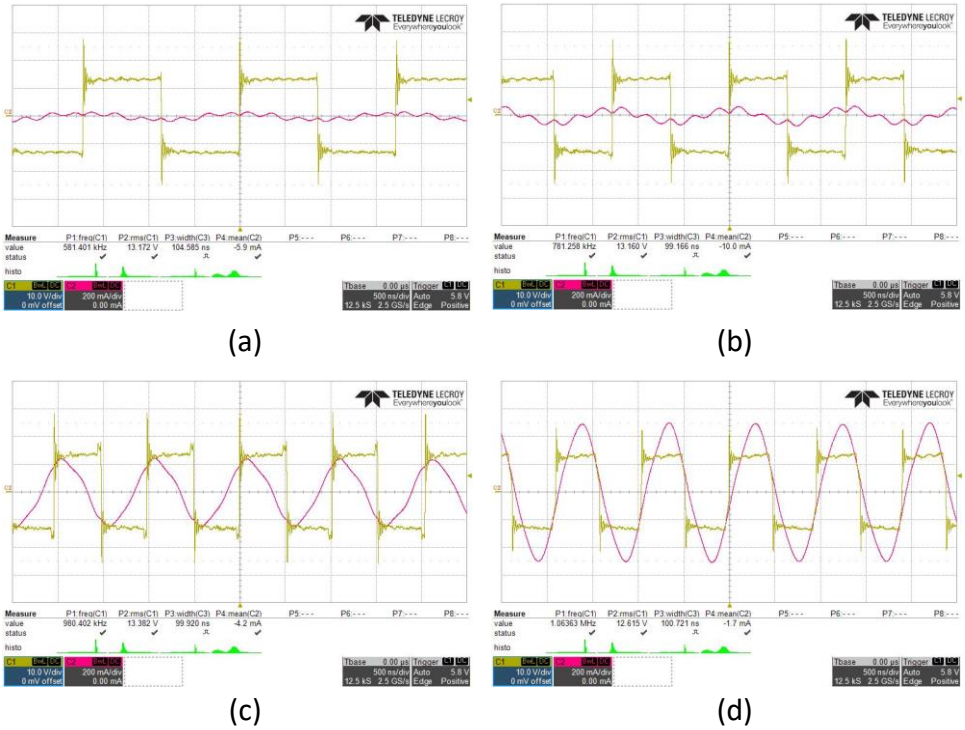

Fig. 49. (a-d) Resonance Tracking Procedure; Yellow- V_p, Red- I_p

Fig. 49 (d). shows that the current signal is slightly leading the voltage signal. Such work-mode ensures soft-switching conditions that minimize switching noises and losses. Once the system is in resonance (or slightly above), the resonance tracking loop enables the current loop to operate. Unlike the start-up frequency tuning (which depends on how far off the resonant frequency is from the initial drive frequency), once the controller is locked into resonance it retains its state, while all the other changes (both electrical and mechanical) are taking place slower.

5.3 Current loop:

The CPT system presented acts as a controlled current source, which implies that the current loop monitors the current at the coupling plates by tuning the L_p, L_s inductance to obtain the target current. The coupling plates' current is sensed via serial resistor, then rectified and transformed into a digital pulse. The received pulse's length is compared to the target pulse, and the controller sets a new target I_{bias} that eventually modifies L_p and changes the output current,

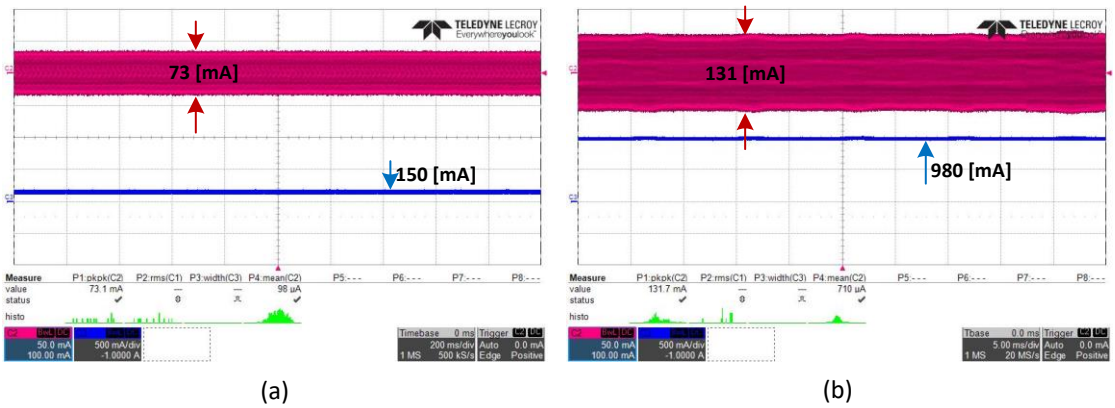

Fig. 50. Blue- I_{bias}, Red- Coupling Capacitor Current (a) Initial State; (b) Final State

as shown in Fig. 50. In can be seen that the red trace in Fig. 50(b) has a minor ripple compared to Fig. 50(a). This occurs due to active compensation when the system enters a more demanding work-mode, but the current ripple is less than 5mA.

5.4 Overall System Dynamics:

As all the control loops were verified experimentally to demonstrate the total system control dynamics and power transfer capabilities, the experimental prototype was tested for a target output power of 10W.

Table 2: Experimental Prototype Parameters at Nominal Operation

Parameter	Value/ Type
V_{in}	30 [V]
I_{out}	1 [A]
Coupling Plates	30x30cm
Air-Gaps	15-100mm
Power Stage	LMG5200, 80 V, 15 mΩ, Dual
Variable Inductors L_p, L_s	~75 [uH]
Capacitor C_p, C_s	, TDK 810 series
Operating Frequency	1.2MHz

Table 2 summarizes the experimental setup parameters at nominal operating conditions. The experimental results of the multi-loop tuning process are shown in Fig. 51. Fig. 51(a) shows the tuning process by means of I_p current at the transmitter and V_s voltage at the receiver, for $V_{in}=30V$. It can be observed that while the system is out of tuning, I_p current has a higher peak value than the corresponding value at the end of the tuning procedure, whether as the V_s voltage at the receiver doesn't satisfy the required output power demand.

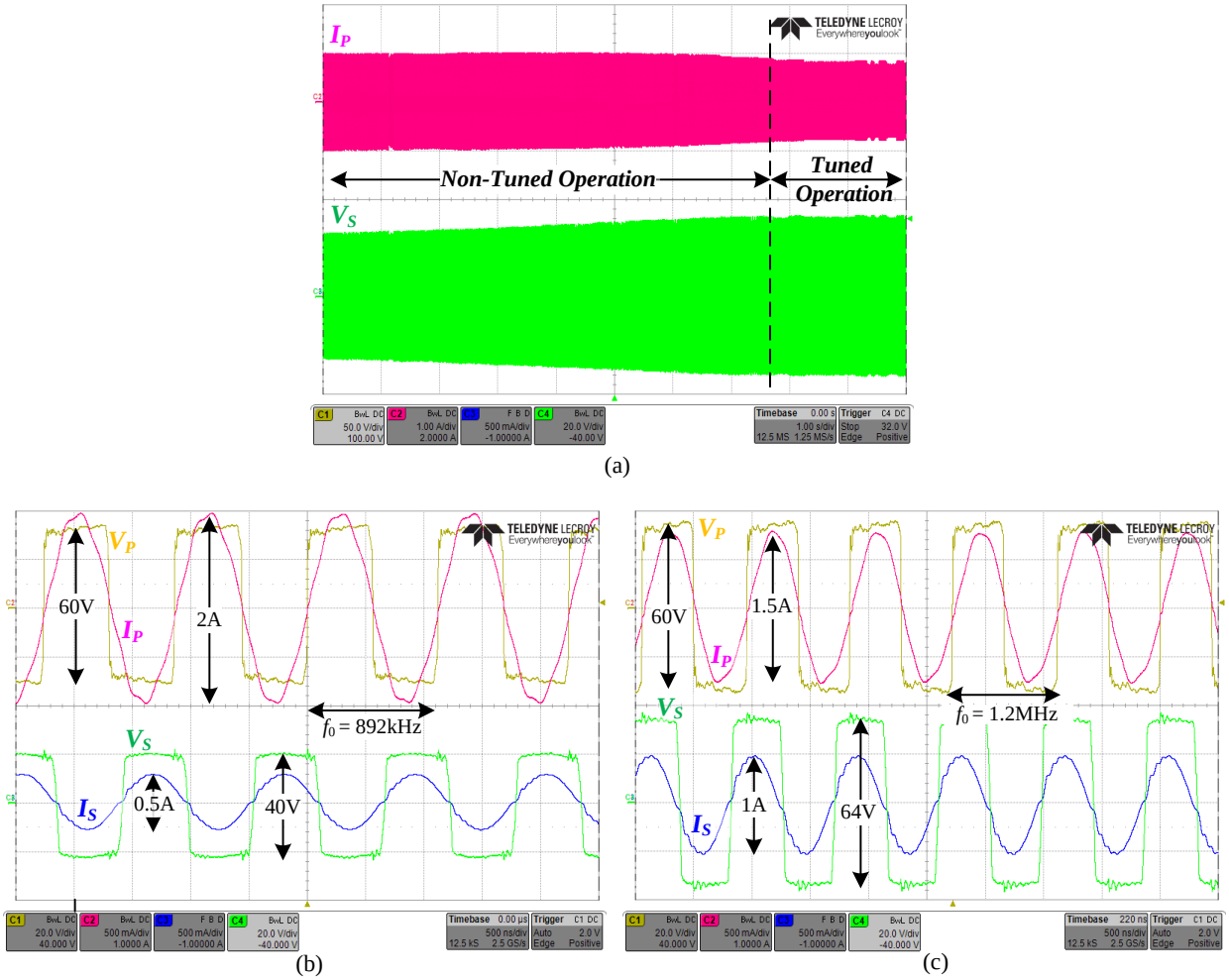

Fig. 51. Experimental results of the tuning process: (a) Full view of the envelopes of IP and VS; (b) Zoom-in view on the initial stage; (c) Zoom-in view on the final stage. Voltage scale 20V/div; Current scale 500mA/div; Time scale 500ns/div

Fig. 51(b), Fig. 51(c), show a zoomed-in views of the initial and final states of the tuning procedure with the voltage and current waveforms at the transmitter and the receiver. It can be seen that as the switching frequency increased from 892 kHz to 1.2 MHz, the power delivered to the load is increased by a factor of 2.5, whereas the transfer efficiency is 4.5 times as high.

5.5 Varying C_m, Varying R_{load} Response:

To further demonstrate the effectiveness of the multi-loop control mechanism, the CPT system was tested under various C_m and R_{load} conditions. Since the presented CPT system acts as a current source, the output power follows $\sim I_s^2 R_{load}$. Therefore, for a fixed I_{ref} at the primary and varying R_{load} at the secondary, the output power may be different from the target power. Due to the lack of access to the receiver side, the 10W output target is achieved by manually regulating I_{ref} at the primary to yield a 10W output (according to a look-up table). Future work overcomes this limitation by adding a wireless communication module. The R_{load} values range from 25Ω to 250Ω as shown in Fig. 52 (a). Varying C_m conditions were tested by changing the air-gap between

the coupling capacitors' plates from 15mm to 100mm, which corresponds to a C_m of 25 pF to 5 pF, with a constant R_{load}=100Ω, as shown in Fig. 52 (b).

In high-Q resonant converter with adaptive resonant tanks, a target value of any of the control parameters (e.g. phase shift, currents, drive frequency etc.) is usually being examined over a range. Hence, the minor change in P_{out} as observed at different R_{load} or C_m values is accounted for by these pre-set limits. These ranges is set in a way that guarantees target output power for a wide range of R_{load} and C_m. Nevertheless, the output power is 10W±0.3W. For a commercial product these ranges can be shrunk in line with the goal application.

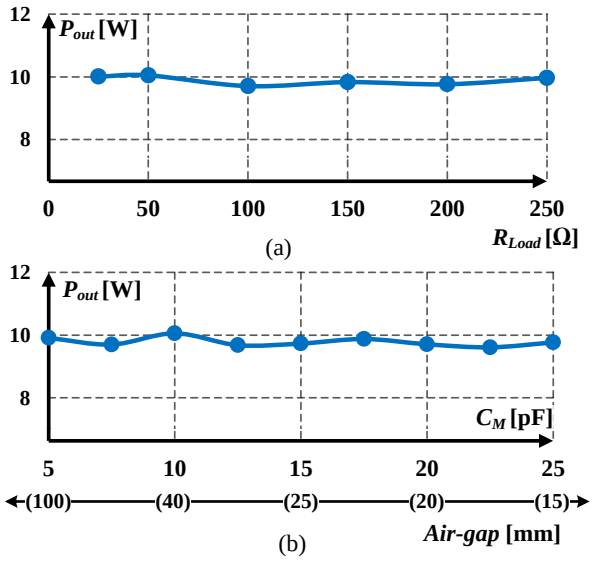

Fig. 52. Measured output power for various: (a) Output loads, (b) Coupling capacitance CM

6 Contribution of This Work and Future Work

6.1 Contribution of This Work

A resonant Capacitive Power Transfer system with an adaptive resonant tank regulated by a multi-loop controller was detailed, analyzed and experimentally verified in this work. The system maintains its current source behavior over a wide range of load resistances and various coupling capacitances, therefore proving the control mechanism functionality.

From research perspective, our study mainly investigated the adaptive control algorithms for CPT systems based on a general double-sided LC system structure. The control mechanism developed addressed the circuit as a series resonance with parallel loading only. The same control mechanism can be applied (fully or partially) to other CPT topologies or IPT systems, as it only utilizes general behavioral properties and measurements in order to perform. For example, changing a double-sided LC CPT system to a double-sided LC IPT system is achieved by a simple replacement of the coupling plates to a coupling (transmitting) coil, leaving waveforms and resonant behavior intact. Moreover, the algorithm of the adaptive resonant tank - combined with the frequency control - can be implemented not only in WPT systems, but also in various resonant DC-DC converters, especially ones of isolated nature.

From a design point of view, the prototype that demonstrates the system's capabilities produces several measurements acquiring and processing methodologies. Although most of the building blocks for sensing and processing were discussed in previous works, their implementation posed serious challenges. The creative solutions to the design challenges in this study can be further implemented in other systems. The uniqueness of the project lies in the observation that the system at hand (besides including several floating ground levels due to FB power stage and single supply sensing demands) combines high frequency, high voltage and high Q parameter in a single circuit. Moreover, all of the abovementioned parameters can change drastically, while the only constant parameter is the input voltage. This high level of uncertainty produced robust tools that can be implemented in other systems.

Experimental results can be leveled-up by improving the initial layout of the boards (lowering unnecessary parasitics, for example) and using materials compatible with high frequency operation. Additionally, a controller with higher inner clock may increase the overall bandwidth and tuning time, while lowering the signals ripple.

Embedding our system into practical applications may reveal additional restrictions that have not been taken into consideration in our study. The following future-work section therefore discusses factors like constant drive frequency and ways to fit the system into emerging standards.

6.2 Future Work

The following part covers the future improvements to the system, planned according to current system limitations:

6.2.1 Variable Capacitance (Fully adaptive matching network)

The adaptive resonant tank presented in this work is tuned by changing the effective inductance of the resonant tank at the transmitter and the receiver. Adhering to the same principle, in order to extend the versatility of the controller and add one more degree of freedom (in terms of control parameters) the parallel capacitors C_p, C_s can be replaced with variable capacitors or with a controlled decade of capacitors. Unlike the CPT system in which tuning L_{res} results in changes in f_{res} and the Q- factor of the resonant tank, applying both variable inductor and capacitors at the resonant tank significantly improves the total system capabilities, by virtue of the many Q-factors obtained at different frequencies. Furthermore, the fully tunable resonant tank solves the problem of system restriction by a constant frequency drive, as it allows to change the transfer function without changing the resonant frequency. For example, for a given state, doubling the capacitance and cutting the inductance by half preserves the resonant frequency, while increasing Q by a factor of 2. It is important to note that since voltage/current controlled capacitors - rated at high voltage - are quite rare, selecting a discrete capacitance is a viable option. Fig. 53 shows the parallel connection of N capacitors, each followed by a switch. The configuration increases the capacitance span from 1 to 2^N (for capacitors of increasing value).

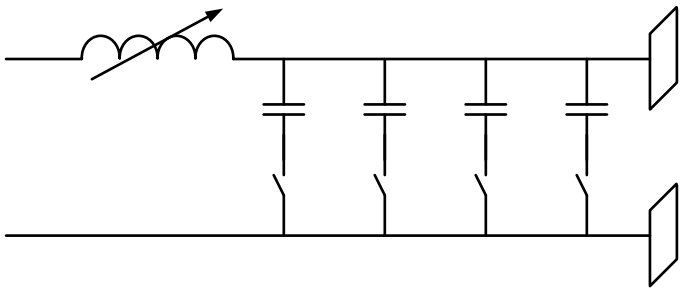

Fig. 53. Variable Capacitance Implementation

6.2.2 Source-Load Communication (Fourth Control Loop)

One of the foremost inherent shortcomings of wireless power transfer systems, including the one presented in this study, is the lack of access to the load. Hence, the control of the output voltage/current/power in such systems is either unmoderated or realized with an additional power conversion stage. One alternative approach is to add a wireless communication component (e.g. Bluetooth). Incorporating the communication module adds fourth control loop to the system that sets I_{ref} value at the transmitter in accordance with the load. In addition to improving the system's current source behavior (as it is done with respect to the actual load

current readings), it also allows a power-supply like behavior. It should also be noted that adding the fourth control loop, which is the outer-most loop, does not change the control dynamics.

6.2.3 Chip

As the experimental prototype is implemented on a PCB that incorporates discrete components and/or modules in order to minimize the system volume and weight, and make the controller commercially attractive the next step. Once accomplished, the total system size will be almost entirely dependent on the size of the coupling plates and the power source.

7 References

[1] E. Abramov, S. Member, A. Mindel, S. Member, M. M. Peretz, "Regulated Power Transfer Using Self-Tuned Networks for Capacitive Wireless Systems."

[2] Wireless Power Consortium, "WIRELESS POWER Introduction to the Power Class 0 Specification," no. February, pp. 1–16, 2017.

[3] AirFuelAllience, "AirFuel Resonant Wireless Power Transfer (WPT) System Baseline System Specifications," pp. 1–88, 2017.

[4] A Treatise on Electricity and Magnetism, Volume 2. Oxford, At The Claredon Press, 1873.

[5] X. Lu *et al.*, "Wireless Charging Technologies : Fundamentals , Standards , and Network Applications," vol. 18, no. 2, pp. 1413–1452, 2016.

[6] D. J. Graham, "Investigation of Methods for Data Communication and Power Delivery Through Metals," no. September, 2011.

[7] G. V. B. Cochran, M. W. Johnson, M. P. Kadaba, F. Vosburgh, and V. R. Palmieri, "Piezoelectric Internal Fixation Devices : A New Approach to Electrical Augmentation of Osteogenesis," no. 1 1, pp. 508–513, 1985.

[8] S. Ozeri, D. Shmilovitz, S. Singer, and C. C. Wang, "Ultrasonic transcutaneous energy transfer using a continuous wave 650 kHz Gaussian shaded transmitter," *Ultrasonics*, vol. 50, no. 7, pp. 666–674, 2010.

[9] X. Bao *et al.*, "Proceedings of spie," no. March 2008, 2019.

[10] K. Jin and W. Zhou, "Wireless Laser Power Transmission: A Review of Recent Progress," *IEEE Trans. Power Electron.*, vol. PP, no. c, p. 1, 2018.

[11] C. Engineering and S. B. Ny, "Power Sensor Networks by Wireless Energy - Current Status and Future Trends," pp. 648–652, 2015.

[12] A. Cai, A. Pereira, R. Tanzania, Y. K. Tan, and L. Siek, "A high frequency, high efficiency GaN HFET based inductive power transfer system," *Conf. Proc. - IEEE Appl. Power Electron. Conf. Expo. - APEC*, vol. 2015–May, no. May, pp. 3094–3100, 2015.

[13] L. Chen *et al.*, "Double-Coupled Systems for IPT Roadway Applications," *IEEE J. Emerg. Sel. Top. Power Electron.*, vol. 3, no. 1, pp. 37–49, 2015.

[14] O. Knecht, S. Member, R. Bosshard, S. Member, and J. W. Kolar, "High-Efficiency Transcutaneous Energy Transfer for Implantable Mechanical Heart Support Systems," *IEEE Trans. Power Electron.*, vol. 30, no. 11, pp. 6221–6236, 2015.

[15] A. Resonant and W. Power, "AirFuel Resonant Wireless Power Transfer (WPT) System Baseline," pp. 1–88, 2017.

[16] J. Lin, Y. Hsieh, and H. Chiu, "High-efficiency Wireless Power Transfer System," *2015 IEEE Int. Telecommun. Energy Conf.*, pp. 1–3.

[17] H. H. Wu, A. Gilchrist, K. D. Sealy, and D. Bronson, "A high efficiency 5 kW inductive charger for EVs using dual side control," *IEEE Trans. Ind. Informatics*, vol. 8, no. 3, pp.

585–595, 2012.

[18] R. Bosshard, S. Member, and J. W. Kolar, "for 50 kW / 85 kHz Automotive IPT System," *IEEE J. Emerg. Sel. Top. Power Electron.*, vol. 5, no. 1, pp. 419–431, 2017.

[19] Z. Wang, X. Wei, and H. Dai, "Design and control of a 3 kW wireless power transfer system for electric vehicles," *Energies*, vol. 9, no. 1, 2016.

[20] G. A. Covic and J. T. Boys, "Modern trends in inductive power transfer for transportation applications," *IEEE J. Emerg. Sel. Top. Power Electron.*, vol. 1, no. 1, pp. 28–41, 2013.

[21] H. H. Wu, I. Member, and J. Boys, "A Practical 1 . 2kW Inductive Power Transfer Lighting System using AC Processing Controllers," *2011 6th IEEE Conf. Ind. Electron. Appl.*, pp. 345–350, 2011.

[22] J. H. Kim *et al.*, "Development of 1-MW Inductive Power Transfer System for a High-Speed Train," *IEEE Trans. Ind. Electron.*, vol. 62, no. 10, pp. 6242–6250, 2015.

[23] V. Cirimele and I. S. Member, "Inductive power transfer for automotive applications : state-of-the-art and future trends," *2016 IEEE Ind. Appl. Soc. Annu. Meet.*, pp. 1–8, 2016.

[24] T. Zhao, B. Pahl, J. Xu, B. Wu, P. Nirantare, and M. Kothekar, "Optimal operation point tracking control for inductive power transfer system," *2015 IEEE Wirel. Power Transf. Conf. WPTC 2015*, pp. 1–4, 2015.

[25] A. Banerji and S. M. Ieee, "Wireless Transfer of Power : Status and Challenges," *2016 Int. Conf. Intell. Control Power Instrum.*, pp. 251–257, 2016.

[26] Y. Li, S. Member, R. Mai, L. Lu, Z. He, and S. Member, "Active and Reactive Currents Decomposition-Based Control of Angle and Magnitude of Current for a Parallel Multiinverter IPT System," *IEEE Trans. Power Electron.*, vol. 32, no. 2, pp. 1602–1614, 2017.

[27] S. Samanta and S. Member, "Dynamic Modelling and Closed Loop Control of Transmitter Parallel and Receiver Series Compensated IPT Topology for EV Applications," pp. 342–347, 2018.

[28] Y. Li, H. Du, M. Yang, and Z. He, "Two-Degree-of-Freedom H∞ Robust Control Optimization for the IPT System with Parameter Perturbations," *IEEE Transactions on Power Electronics*, vol. 33, no. 12. pp. 10954–10969, 2018.

[29] C. Tang, Z. Gu, H. Shen, Y. Li, and Z. Xu, "Dynamic characteristics optimization control method for Buck-IPT system," *2017 IEEE PELS Work. Emerg. Technol. Wirel. Power Transf. WoW 2017*, pp. 320–324, 2017.

[30] S. Nutwong, A. Sangswang, and S. Naetiladdanon, "Output voltage control of the SP topology IPT system using a primary side controller," *2016 13th Int. Conf. Electr. Eng. Comput. Telecommun. Inf. Technol. ECTI-CON 2016*, pp. 1–5, 2016.

[31] J. Dai and D. C. Ludois, "A Survey of Wireless Power Transfer and a Critical Comparison of Inductive and Capacitive Coupling for Small Gap Applications," *IEEE Trans. Power Electron.*, vol. 30, no. 11, pp. 6017–6029, 2015.

[32] C. Liu, S. Member, A. P. Hu, S. Member, and M. Budhia, "A Generalized Coupling

Model for Capacitive Power Transfer Systems," pp. 274–279, 2010.

[33] H. Zhang *et al.*, "A Loosely Coupled Capacitive Power Transfer System with LC Compensation Circuit Topology," 2016.

[34] F. Lu, H. Zhang, and C. Mi, "energies on the Recent Development Development of of Capacitive," 2017.

[35] M. N. H. Nishiyama, "Form and Capacitance of Parallel-Plate Capacitors," *IEEE Trans. components, Packag. Manuf. Technol. part A*, vol. 17, no. 3, pp. 477–484, 1994.

[36] J. Dai and D. C. Ludois, "Single active switch power electronics for kilowatt scale capacitive power transfer," *IEEE J. Emerg. Sel. Top. Power Electron.*, vol. 3, no. 1, pp. 315–323, 2015.

[37] J. Dai, S. Member, D. C. Ludois, and M. Ieee, "Wireless Electric Vehicle Charging via Capacitive Power Transfer Through a Conformal Bumper," *2015 IEEE Appl. Power Electron. Conf. Expo.*, pp. 3307–3313, 2015.

[38] J. Jang, W. Chae, H. Kim, D. Lee, and H. Kim, "A study on Optimization of the wireless power transfer using the half-bridge flyback converter," *2010 Second Int. Conf. Comput. Res. Dev.*, pp. 717–719.

[39] M. Kline, I. Izyumin, B. Boser, and S. Sanders, "Capacitive power transfer for contactless charging," *Conf. Proc. - IEEE Appl. Power Electron. Conf. Expo. - APEC*, pp. 1398–1404, 2011.

[40] M. P. Theodoridis, "Effective capacitive power transfer," *IEEE Trans. Power Electron.*, vol. 27, no. 12, pp. 4906–4913, 2012.

[41] B. Yang, R. Chen, and F. C. Lee, "LLC Resonant Converter for Front End DC / DC Conversion Alpha J . Zhang and Guisong Huang," vol. 00, no. c, pp. 346–351, 2002.

[42] F. Musavi, M. Craciun, D. S. Gautam, W. Eberle, and W. G. Dunford, "An LLC resonant dc-dc converter for wide output voltage range battery charging applications," *IEEE Trans. Power Electron.*, vol. 28, no. 12, pp. 5437–5445, 2013.

[43] S. Sinha, A. Kumar, and K. K. Afridi, "Active variable reactance rectifier-A new approach to compensating for coupling variations in wireless power transfer systems," *2017 IEEE 18th Work. Control Model. Power Electron. COMPEL 2017*, 2017.

[44] X. Wang, Y. W. Li, S. Member, and F. Blaabjerg, "Virtual-Impedance-Based Control for Voltage-Source and Current-Source Converters," vol. 30, no. 12, pp. 7019–7037, 2015.

[45] I. Transactions and O. N. Power, "A Comparison of Half-Bridge Resonant Converter Topologies," vol. 3, no. 2, pp. 174–182, 1988.

[46] E. Abramov, S. Member, and M. M. Peretz, "Modeling and Analysis of Capacitive Wireless Power Transfer Systems : A Network Approach," *2018 IEEE Int. Power Electron. Appl. Conf. Expo.*, pp. 1–6.

[47] T. Vekslender, E. Abramov, Y. Bezdenezhnykh, A. Cervera, and M. M. Peretz, "Full IC design of a PWM controller with integrated high-resolution ADC and DPWM peripherals using digital backend tools," *2014 IEEE 28th Conv. Electr. Electron. Eng. Isr.*

IEEEI 2014, pp. 1–5, 2014.

[48] M. M. Peretz and S. Ben-Yaakov, "Digital control of resonant converters: Frequency limit cycles conditions," *Conf. Proc. - IEEE Appl. Power Electron. Conf. Expo. - APEC*, pp. 1704–1708, 2009.

[49] M. M. Peretz and S. Ben-Yaakov, "Digital control of resonant converters: Resolution effects on limit cycles," *IEEE Trans. Power Electron.*, vol. 25, no. 6, pp. 1652–1661, 2010.

[50] M. M. Peretz, S. Ben-yaakov, "Digital Control of Resonant Converters : Enhancing Frequency Resolution by Dithering," pp. 1202–1207, 2009.

[51] Y. Bezdenezhnykh, T. Vekslender, E. Abramov, A. Cervera, and M. M. Peretz, "Design and IC implementation of a fully digital power management delay-line ADC," *2014 IEEE 28th Conv. Electr. Electron. Eng. Isr. IEEEI 2014*, pp. 1–5, 2014.

[52] D. Medini and S. Ben-yaakov, "A Current-Controlled Variable-Inductor for High Frequency Resonant Power Circuits," vol. 2, no. 2, 1994.

[53] O. Ezra and M. M. Peretz, "Combined current sensor and non-invasive displacement measurement for magnetic actuators," *2014 IEEE 28th Conv. Electr. Electron. Eng. Isr. IEEEI 2014*, pp. 1–5, 2014.

[54] I. International and E. Safety, *IEEE Standard for Safety Levels with Respect to Human Exposure to Radio Frequency Electromagnetic Fields, 3kHz to 300 GHz*, vol. 2005, no. April. 2006.